

12-2018

3D SCINTILLATOR DETECTOR QUENCHING CHARACTERIZATION FOR SCANNING PROTON BEAMS

Fahed Alsanea

Follow this and additional works at: https://digitalcommons.library.tmc.edu/utgsbs_dissertations



Part of the [Medicine and Health Sciences Commons](#), and the [Other Physics Commons](#)

Recommended Citation

Alsanea, Fahed, "3D SCINTILLATOR DETECTOR QUENCHING CHARACTERIZATION FOR SCANNING PROTON BEAMS" (2018). *The University of Texas MD Anderson Cancer Center UTHealth Graduate School of Biomedical Sciences Dissertations and Theses (Open Access)*. 917.
https://digitalcommons.library.tmc.edu/utgsbs_dissertations/917

This Dissertation (PhD) is brought to you for free and open access by the The University of Texas MD Anderson Cancer Center UTHealth Graduate School of Biomedical Sciences at DigitalCommons@TMC. It has been accepted for inclusion in The University of Texas MD Anderson Cancer Center UTHealth Graduate School of Biomedical Sciences Dissertations and Theses (Open Access) by an authorized administrator of DigitalCommons@TMC. For more information, please contact digitalcommons@library.tmc.edu.

3D SCINTILLATOR DETECTOR QUENCHING CHARACTERIZATION FOR SCANNING PROTON BEAMS

by

Fahed M Alsanea, M.S.

APPROVED:



Sam Beddar, Ph.D.

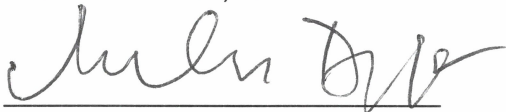
Advisory Professor



Narayan Sahoo, Ph.D.



Gabriel Sawakuchi, Ph.D.



Dragan Mirkovic, Ph.D.



Rajat Kudchadker, Ph.D.



Clifton Fuller, Ph.D.

APPROVED:

Dean, The University of Texas

MD Anderson Cancer Center UTHealth Graduate School of Biomedical Sciences

3D SCINTILLATOR DETECTOR QUENCHING CHARACTERIZATION FOR SCANNING PROTON BEAMS

A

DISSERTATION

Presented to the Faculty of

The University of Texas

MD Anderson Cancer Center UTHealth

Graduate School of Biomedical Sciences

in Partial Fulfillment

of the Requirements

for the Degree of

DOCTOR of PHILOSOPHY

by

Fahed M Alsanea, M.S.

Houston, Texas

December, 2018

Acknowledgments

I would like to thank my advisor Dr. Beddar for his guidance and support in my graduate studies journey. His mentorship and training approach has greatly improved my skills as a scientist. I would like to acknowledge all the members of my advising committee, and examining committee: Dr. Sahoo, Dr. Sawakuchi, Dr. Mirkovic, Dr. Kudchadker, Dr. Howell, Dr. Bankson, and Dr. Fuller. A special thanks to Dr. Sahoo for always supporting my work, helping with experiments at the proton center, and providing key knowledge in proton therapy. Also, a special thanks to Dr. Sawakuchi who have been essential in my research and education.

I would like to thank current and former scintillation lab members: Francois Therriault-Proulx, Landon Wootton, Beckett Hui, Gustavo Kertzscher, Daniel Robertson, Chinmay Darne, Hanen Ziri, Jeppe Christensen, and Rajesh Panthi. Thanks to all my friends in Houston, specially James Eguchi, Daman Grewal, and Jackie Gilberto. Thanks to all the members of the medical physics program and people that have helped and supported me during my graduate studies. Also, I would like to thank the members of the American Legion Auxiliary for their support through the American Legion Auxiliary Fellowship in Cancer Research.

Finally, a special thank you to my mother. The support she provides helped me and my brother and sister to achieve any goal we set.

This work was supported by the National Cancer Institute of the National Institutes of Health (Award Number R01CA182450). The content is solely the responsibility of the authors and does not necessarily represent the official views of the National Institutes of Health.

3D SCINTILLATOR DETECTOR QUENCHING CHARACTERIZATION FOR SCANNING PROTON BEAMS

Fahed M Alsanea, M.S.

Advisory Professor: Sam Beddar, PhD

Proton pencil beam scanning is becoming the standard treatment delivery technique for proton therapy centers. Scanned proton pencil beams provide a highly conformal dose distribution. The complex dose distribution poses challenges for quality assurance measurements leading to sophisticated detector setups and time consuming measurements. Fast 3D measurements are therefore desirable to verify the complex dose distribution and to enable the utilization of the full potential of proton therapy. The overall objective of this project is to improve volumetric scintillator detectors to provide 3D measurements for applications for beam commissioning, quality assurance program, and patient-specific treatment delivery verification.

Detectors based on volumetric scintillators are gaining interest for use in proton therapy because they promise fast and high-resolution proton beam measurements. However, the scintillators' response depends on the ionization density of the incident radiation, termed ionization quenching. For protons and other heavy charged particles, the ionization density, which is quantified as the linear energy transfer (LET), varies as a function of depth. Therefore, quenching introduces a non-linear response to the absorbed dose of proton beams. To fully utilize volumetric scintillator detectors for dose verification, ionization quenching correction factors are needed.

Previous studies have shown the feasibility of using multiple cameras to image volumetric scintillators for obtaining real-time measurements, and 3D information. Furthermore, ionization quenching correction models based on the widely used Birks' equation was shown to have lower dose accuracy at the Bragg peak for low-energy beams. The purpose of this study is to accurately determine

the ionization quenching correction factors and to characterize a novel 3D scintillator detector for scanned proton beams.

The 3D scintillator detector consisted of a liquid scintillator filled tank imaged by three identical sCMOS cameras. The system exhibited a high spatial (0.20 mm) and temporal resolution (10 ms). It was capable of capturing and verifying the range of all the 94 beam energies delivered by the synchrotron with sub-millimeter accuracy. The use of multiple orthogonally positioned cameras allows for detecting the precise locations of delivered beams in 3D. The beam images captured by the detector were synchronized with synchrotron beam delivery trigger signals. The developed image acquisition technique demonstrates the capability of the detector to capture single spots with a reproducible accuracy of 2%. Ionization quenching correction factors were used to correct the response of scintillators for dose linearity. The EDSE scintillation model was explored which relates the scintillation light emission to the energy deposition by secondary electrons.

This project explored key improvements necessary for volumetric scintillator-based detector and demonstrated the capabilities of a novel 3D scintillator detector as a potential comprehensive quality assurance tool and for patient treatment verification detector for spot scanning proton therapy.

Table of Contents

Acknowledgments	iii
Abstract	iv
Table of Contents	vi
List of Illustrations	x
List of Tables	xiii
Chapter 1 : Introduction	1
1.1 Purpose statement	2
1.2 Rational and significance	2
1.3 Hypothesis	3
1.4 Specific aims	3
1.4 Dissertation organization	5
Chapter 2 : Background	6
2.1 Proton Therapy	7
2.2 Proton Beam Delivery	8
2.3 Proton Therapy Quality Assurance	9
2.4 Dosimeters for proton therapy QA	9
2.5 Scintillation dosimetry	10
2.6 Ionization quenching	12
Chapter 3 : 3D scintillator detector characterization	15

3.1. Introduction.....	16
3.2. Methods and materials	18
3.2.1. Design of the 3D detection system	18
3.2.2. Optical system design.....	21
3.2.3. Optical artefact corrections.....	21
3.2.4. Spatial resolution.....	22
3.2.5. Camera linearity	22
3.2.6. Camera stability.....	23
3.2.7. Proton range measurement accuracy	23
3.2.8. Lateral beam profiles.....	25
3.2.9. Determining 3D beam locations.....	25
3.3. Results	26
3.3.1. Spatial resolution.....	26
3.3.2. Camera linearity	27
3.3.3. Camera stability.....	27
3.3.4. Proton range measurement accuracy	29
3.3.5. Lateral beam profiles.....	31
3.3.6. 3D beam locations.....	34
3.4. Discussion	36
3.5. Conclusion	37
Chapter 4 : Spot scanning camera synchronization	38

4.1. Introduction.....	39
4.2. Methods	40
4.2.1. Proton beam system	40
4.2.2. Cameras	41
4.2.3. Camera Triggering	43
4.2.4. Beam delivery settings: trigger testing.....	46
4.3. Results	48
4.4. Discussion	52
4.5. Conclusion	54
Chapter 5 : Ionization Quenching Correction factors.....	55
5.1. Introduction.....	56
5.2. Methods	57
5.2.1 3D Scintillator Detector	57
5.2.2 Irradiation conditions and Monte Carlo Simulations	58
5.2.4 Quenching Correction	60
5.2.5 Quenching Correction factor	63
5.3. Results	63
5.3.1 Optical Corrections	63
5.3.2 Quenching Model fitting	65
5.3.3 Quenching correction factors.....	67
5.4. Discussion	68

5.5. Conclusion	69
Chapter 6 : Conclusions and future directions	71
6.1. Summary and Conclusions	72
6.2. Future Directions	73
Bibliography.....	75
Vita	80

List of Illustrations

Figure 2.1 Depth profile plot of a 161.6 MeV proton pencil beam in water.	8
Figure 2.2 a) A schematic of a proton track interacting with matter, resulting in a shower of secondary electrons b) Electron energy deposition density per unit path length of the incident ion beam (proton 98.6 MeV) as a function of the radial distance from the ion's track (solid line). The EDSE model assumes a region close to the ion's track (core region) where the scintillator quenches (red dotted line).	13
Figure 3.1 (a) Photograph of the 3D liquid scintillator detector setup placed on a patient couch in a discrete spot scanning proton beam gantry. (b) Integrated light profiles of a proton beam captured using the three-camera setup.	19
Figure 3.2 Schematic of the 3D liquid scintillation detector. (a) 3D model of the system. (b) Right-side view of the detector system with cameras X and Y imaging the scintillation volume. A 45° mirror mounted on the top of the volume redirected scintillation light to camera Y. Camera Z and side mirror are not shown in the 2D schematic for simplicity.	19
Figure 3.3 (a) Normalized depth scintillation light profiles for five beam energies measured with camera X. (b) Normalized lateral scintillation light profiles of the same beam energies. On both figures, the x-axis shows the location of the Bragg peak with respect to the center of the tank volume.	26
Figure 3.4 Spatial resolution of the detection system as a function of working distance from the camera sensor plane to different imaging planes within the scintillation volume. The change in resolution was modeled using a linear fit.	28
Figure 3.5 (a) Linear response of the camera to increasing dose for 161.6 MeV beam energy. (b) Signal-to-noise of camera X as a function of the delivered dose (Gy).	29
Figure 3.6 (a) Proton-beam range-measurement accuracy plotted for all 94 energies delivered by the synchrotron. The difference between the measured (R_{measured}) and reference ($R_{\text{reference}}$) beam ranges is plotted as a function of their range inside the tank volume. The energies were delivered in two batches: low-energy (72.5-141.6 MeV) and high-energy (129.2-221.8 MeV). (b) Uncertainty in range	

measurements for low-dose deliveries. Uncertainty in measurements is represented by the error bars in both the figures.	31
Figure 3.7 (a) Lateral 1D integrated light profile recorded by camera X is compared to Monte Carlo simulation of lateral dose profile at depth $z = 20$ mm from the entrance of the scintillation volume. (b) Lateral 1D integrated light profiles of spots of single beam energies incident at different locations from the central axis ($y_{\text{shift}} = 0$ cm) along the y-axis ($y_{\text{shift}} = \pm 4$ cm and ± 8 cm) are shown.	33
Figure 3.8 Lateral 1D deconvolved integrated light profile recorded by camera X (dashed line) is compared to Monte Carlo simulation (solid line) of lateral dose profile at Bragg peak for 161.1 MeV, 144.0 MeV, 100.9 MeV, and 85.6 MeV.	34
Figure 3.9 Spot location accuracy calculated as the difference between measured and programmed beam locations inside the scintillation volume is plotted for a beam energy of 161.6-MeV (nominal location of 60.85 mm within the scintillation volume) and for the beam locations, (0,0), (± 4 cm,0), (0, ± 4 cm), in the (a) z-projection, and (b) x-projection.	35
Figure 4.2 A flowchart describing the camera triggering and proton spot counting scheme developed in this study.	45
Figure 4.3 Timing diagram of the sCMOS trigger synchronization with synchrotron-generated signals (START and STOP) and dose monitor pulses. This example shows 2 energy layers with 4 spots each. The trigger is set to capture 2 spots in a frame. The camera readout shows the signal frames (S) and reference frames (R).....	46
Figure 4.4 The processed integrated depth dose curves (projection X or Y) and lateral profiles (projection Z) as captured by the scintillator detector.	49
Figure 4.5 The percentage difference between trigger and non-trigger modes as a function of the SNR for the 10.247 ms frame. The errorbars represent the standard deviation over 5 measurements.	50
Figure 4.6 Normalized mean intensity of 2 spots (0.08 MU) in an image which was repeated 4 times in a run per location. The experiment was performed 3 times resulting in a total of 15 images per location	

for each of the 5 beam energies. The results shown are for camera X. The signal was normalized to the middle spot of the 3 spot locations along the x-axis. The other 2 cameras showed similar response.....	51
Figure 4.7 Intensity difference between triggered and non-triggered acquisition for Camera Z exposed to 161.6 MeV beam as a function of pixel intensity. The overlap region of the two ADCs is around 4000 a.u.	54
Figure 5.1 A schematic of integrated depth dose (IDD) measurements compared to the scintillator projections. The IDD measurements present an orthogonal projection of the dose, while the scintillator detector projections are displaced due to the use of an objective lens. The scintillator projections are a result of integrating along a different volume depending on the location of the beam.	60
Figure 5.2 a) The depth dose profile of a 100.9 MeV proton beam, along with the scintillation light and LET curves. b) The corresponding projection from the 3D scintillator detector (z-y plane, projection x).	64
Figure 5.3 The central axis depth dose curves of the measured scintillation signal for the original projections of the 3D scintillator detector and shifted projections that align the Bragg peak at the center of the camera. The Bragg peak central projections are sharper than the original projections.	65
Figure 5.4 The measured scintillation light signal as a function of LET for proton beam energies along with the curve fitting using Birks semi-empirical model. a) plots the measured scintillation signal of the original projections (filled markers) and the Bragg peak central projections. b) shows the scintillation signal of the original projections as a function of LET that have been averaged along the central axis according to the parallax displacement.	66
Figure 5.5 (Top) The depth-dose profiles at the central axis for each proton beam energy. The dose calculated using MC simulation is compared to the corrected and uncorrected scintillation signal using the Birks model and EDSE model. (Bottom) The ratio of the MC dose (D_{MC}) to corrected dose of the scintillator (D_s) for both models tested in this study.	67

List of Tables

Table 4.1 The mean percentage difference in the mean intensity measured using trigger mode and non-trigger mode for 5 proton beam energies with 50 spots per energy. The measurements were performed 3 times.	49
Table 4.2 Background signal measurements for different exposure times. The percentage increase was calculated relative to the 1-ms exposure time measurement.	52
Table 5.1 The percent difference from Monte Carlo of the Bragg peak height for each beam energy using the Birks and EDSE quenching correction factors.....	68

Chapter 1 : Introduction

1.1 Purpose statement

The purpose of this project is to characterize and determine the ionization quenching of volumetric organic scintillators for scanned proton beams. Volumetric scintillator detectors promise to measure complex treatment plan dose distribution for proton therapy. However, the response of scintillators depends on the ionization density of the interacting radiation type. To enable the use of volumetric scintillators in proton therapy the ionization quenching phenomenon must be addressed.

1.2 Rational and significance

Radiotherapy for cancer treatment has seen great advancement to increase dose conformity. Proton therapy treatment plans are an excellent example of plans that can deliver complex conformal dose distribution to the targeted cancer while sparing surrounding healthy tissue beyond the finite range of the proton beam (Bragg peak region). However, one of the main challenges of such complex treatment plans, in particular in intensity modulated proton therapy (IMPT) treatment plans, is dose verification. Current standard radiation measurement technologies rely on point detectors or 2D arrays to perform quality assurance (QA), which results in time consuming measurements (Zhu *et al* 2011, Karger *et al* 1999). However, 3D measurements are desirable to verify the complex dose distribution and enable utilization of the potential advantages of proton therapy. While there are 3D detectors like gel and radiochromic dosimeters, they are single use detectors that do not provide real time readout (Baldock *et al* 2010).

We have developed a large volume organic liquid scintillator detector that has the capability to image 3D dose distributions of proton beams in real time (Beddar *et al* 2009, Darne *et al* 2017). It will provide patient specific treatment dose verification faster than current technology used in the clinic. In organic scintillators, the energy absorbed is emitted as visible light that can be captured using optical cameras. However, the scintillation light emission exhibits a non-linear response with the incident radiation ionization density. For proton and heavy charged particles, the ionization density, which is

quantified as the linear energy transfer (LET), varies as a function of depth. The LET increases rapidly at the Bragg peak region and corresponds to a diminished light emission by the organic scintillator. This phenomenon is called ionization quenching and it must be addressed to utilize 3D scintillator detectors for dose verification. Earlier results by our group demonstrated that quenching correction was possible using Birks equation (Birks 1964), but the errors between the corrected light signal and the calculated dose were $\pm 5\%$ (Wang *et al* 2012, Robertson *et al* 2013). For IMPT plans we need an improved dose accuracy for detecting treatment plan errors used in patient treatment because tumor-control and normal-tissue complication probabilities are steep functions of absorbed dose (ICRU, 2008).

1.3 Hypothesis

Our long-term goal for this project is to improve the accuracy of treatment verification using 3D scintillator detector and reduce treatment errors. The objective is to accurately measure the ionization quenching for volumetric organic scintillators and develop quenching correction models for clinical applications. We hypothesize that semi-empirical modeling of the mechanism of quenching in organic scintillators exposed to proton beams will correct the measured light emission in the 3D scintillator detector to obtain dose accuracy less than 3% in any clinical proton radiation field. The rationale for this project is to further expand the understanding of the ionization quenching mechanism because it will enable the use of volumetric scintillators for high-resolution 3D dose verification, resulting in a detector that will allow real time verification of 3D dose distribution

1.4 Specific aims

This project was conducted in three specific aims. Each aim tackled a separate aspect to improve and utilize volumetric scintillators for proton therapy.

The first aim was to determine the 3D scintillator detector characteristics. The 3D scintillator detector design was tested for its ability to produce accurate dose distribution. This characterization

was used to demonstrate the capabilities of the 3D scintillator detector for quality assurance program in proton therapy.

The second aim was to synchronize image acquisition with proton beam deliveries. The beam delivery of proton therapy using a synchrotron based accelerator is dynamic. The beam spots are delivered in a short bursts of time (in the order of milliseconds) at specific locations for a patient treatment plan. This aim will provide a methodology to capture dynamic beam delivery with better efficiency to capture single spots. The trigger system was tested to capture individual proton spots with high reproducible accuracy. The synchronized triggering system simplified and improved light measurement analysis for ionization quenching correction.

The third aim was to develop methodology to correct for ionization quenching. We determined and corrected the ionization quenching by measuring the light distributions produced in the 3D scintillator detector by exposing it to proton beams. The ionization quenching correction included models based on LET and radial dose distribution (RDD) of the proton beam. We modified the present Energy Deposition by Secondary Electron (EDSE) model for use in correcting ionization quenching in volumetric scintillators. The working hypothesis is that modelling the mechanism of quenching at the microscopic level (EDSE model) will provide more accurate quenching correction factors than the well-established model to correct the measured light projections. Models related to secondary electron spectrum have never been applied to volumetric scintillators for radiotherapy dose verification. The outcome of this aim will provide a semi-empirical model that will correct for ionization quenching in volumetric scintillator exposed to any proton beam energy.

The outcome of this work will introduce accurate quenching correction factors for 3D scintillator detectors, which will improve the accuracy of dose verification in patient treatment plan quality assurance with the additional advantage of providing real-time information. The study will provide a better understanding of the quenching mechanism for volumetric organic scintillators.

1.4 Dissertation organization

The following chapter will cover the background information regarding scintillation dosimetry and proton therapy to provide a general understanding of the presented research. Three more chapters will cover the results of the three specific aims listed above. Then, a final chapter will summarize the key findings and discuss the future directions of this research.

Chapter 2 : Background

2.1 Proton Therapy

Proton therapy was proposed back in 1946 by Robert Wilson to treat deep tumors (Wilson 1946). The biophysical rational and techniques of proton beam delivery was explained in the seminal paper by Robert Wilson (Wilson 1946). The first human treated with proton therapy was performed shortly after in 1954 at the Lawrence Berkeley Laboratory (Paganetti 2011). The treatment was of a pituitary gland in a metastatic breast cancer patient for hormone suppression (Tobias *et al* 1958). Since then, proton therapy has advanced considerably. Some major early contributors to proton therapy were from the following institutes, Gustav Werner Institute, Uppsala, Sweden; Harvard University at Harvard Cyclotron Laboratory, Cambridge, Massachusetts; the National Institute for Radiological Sciences in Chiba, Japan; and Loma Linda University Medical Center in Loma Linda, CA.

The rationale for using protons in cancer therapy has to do with their physical interactions with tissue. Depending on their initial energy, protons stop over a narrow depth inside the target, and are therefore able to deliver entirety of the intended dose to that region; called the Bragg peak as shown in figure 2.1. This characteristic of protons helps in providing highly conformal tumor target coverage while sparing adjacent healthy tissues and critical organs. This makes proton therapy a very attractive modality. Currently, there are 81 centers operating worldwide with 43 in development (Particle Therapy Co-Operative Group). The number of patients treated using protons and heavier ions are projected to increase (Durante and Paganetti 2016).

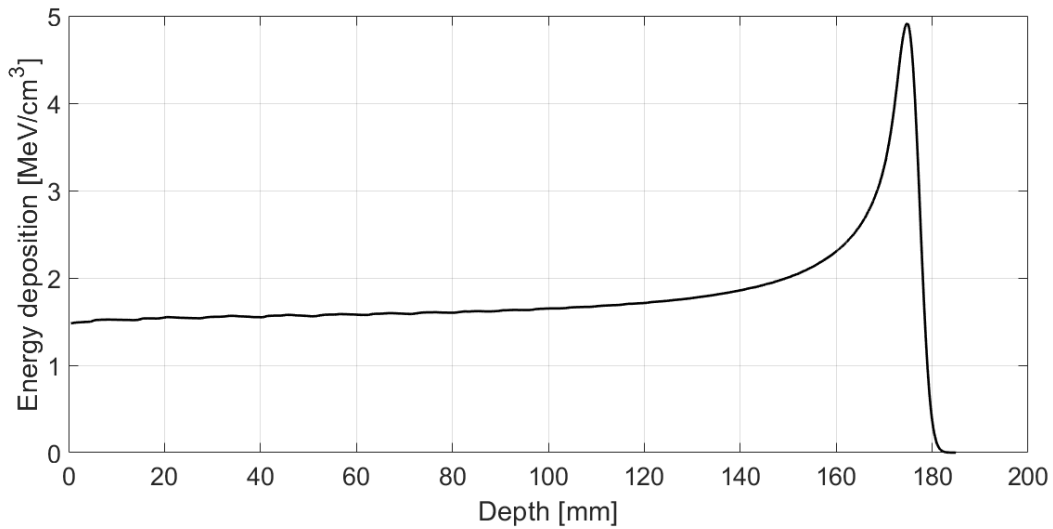


Figure 2.1 Depth profile plot of a 161.6 MeV proton pencil beam in water.

2.2 Proton Beam Delivery

There are two main modern techniques of delivering dose to the target volume using protons. The first technique is passive scattering beam, where the proton beam is spread using scattering and range shifting materials. The scattering material will spread a mono-energetic beam laterally, in which the proton beam width is spread much larger to cover targeted areas with widths in the order of cm. The proton beam is spread axially using a modulator wheel. The modulator wheel will shift a mono-energetic beam to create a combination of beams that will cover a uniform depth dose region, called the spread out Bragg peak (SOBP). The second technique is scanning proton beam, which is becoming increasingly popular because it is capable of delivering a highly conformal dose distribution. The discrete spot scanning proton beam technique utilizes a narrow proton beam, which is termed as 'spot' (or beamlet), that is magnetically steered laterally and modulated in depth by changing the proton's kinetic energy to deliver a three-dimensional (3D) dose distribution. This beam delivery enabled advanced treatment technique such as the intensity modulated proton therapy (IMPT) (Paganetti 2011).

Current proton therapy accelerators are either cyclotrons or synchrotrons. The cyclotron accelerates proton to a fixed beam energy (200-250 MeV), and use a fast energy degrader to change the energy of the beam. Synchrotron technology is advantageous because protons can be accelerated to the desired energy, which results in no radioactivity creation due to beam losses. Also, low energy protons can have the same beam intensity. However, the shape and distribution of the proton beam using a synchrotron system will be different for each proton beam energy (Paganetti 2011).

The published Proton Therapy Physics, edited by Harald Paganetti, includes more information on proton therapy history, beam delivery techniques, quality assurance, etc. (Paganetti 2011).

2.3 Proton Therapy Quality Assurance

A quality assurance (QA) program is vital in any modality of radiotherapy to insure the utmost safety and avoid adverse events resulting from treatment (Pawlicki *et al* 2010). While some aspects of proton radiation therapy are similar to conventional photon or electron therapy, proton therapy poses some additional challenges. These challenges stem from the fact that proton therapy is still relatively new. Furthermore, there are many different systems and beam delivery to choose from. Therefore, a QA program will be unique for each center. Nonetheless, there are requirements to meet. These requirements are acceptance testing, beam commissioning, quality assurance program, and patient specific quality assurance (Pawlicki *et al* 2010). ICRU report 78 (ICRU, 2008) addresses QA measurements for proton therapy, including patient specific QA.

2.4 Dosimeters for proton therapy QA

The ionization chamber is considered the gold standard in radiation measurements. Therefore, it is expected to also be the standard in proton therapy. However, for IMPT treatment plans it is too time consuming to measure the dose distribution with a single ionization chamber. Also, a scanning ionization chamber will not be able to capture the dose distribution due to the nature of proton beam dynamic delivery. Linear arrays of ion chamber detectors were used to improve measurements

efficiency (Karger *et al* 1999, Lomax *et al* 2004, Coray *et al* 2002). Furthermore, commercially available 2D arrays of ionization chambers were used for patient specific QA (Zhu *et al* 2011, Arjomandy *et al* 2010). These detectors exhibit limitations due to the number of points measured in an array, number of measurements depths, and detector spacing. Furthermore, the measurements will suffer from volume averaging effects, which will limit their accuracy in steep dose gradients. Similarly, 2D detectors based on scintillator screens, and gafchromic films can be used for proton therapy QA. Again, they do not provide direct 3D measurements.

The available 3D detectors are not ideal and suffer many limitations. The notable ones are Gel dosimeters and solid radiochromic (Presage) dosimeters (Johansson *et al* 1997, Zhao *et al* 2012, Baldock *et al.*, 2010; MacDougall *et al.*, 2002). Gel dosimeters can be difficult to work with because of their sensitivity to preparation techniques and exposure to oxygen (McJury *et al.*, 2000). A new form of 3D dosimeter, the PRESAGE solid radiochromic dosimeter, eliminates some of these problems (Guo *et al.*, 2006). All of these dosimeters are integrating dosimeters, which are not capable of measuring the temporal variation of dynamic radiation delivery systems. Furthermore, both are single use detectors and require separate readout using CT, optical CT, or MRI scanners, which is time consuming and expensive (Guo *et al* 2006, Zeidan *et al* 2010, Sakhalkar *et al.*, 2009; Lopatiuk-Tirpak *et al.*, 2008). Moreover, the response to dose is not linear in these detectors, so they require additional correction terms (Zhao *et al* 2012).

Karger *et al* describes the advantages and disadvantages of different dosimetry systems for ion beam radiotherapy (Karger *et al* 2010). In the next sections, a short review of scintillator based detectors will be covered.

2.5 Scintillation dosimetry

Scintillators are transparent material that can be in a solid, liquid, or gas state. The interaction of ionizing radiation with scintillators results in the emission of visible light that can be captured using

light sensitive detectors, such as a photomultiplier (PM) tube, and Charge-coupled device (CCD).

Scintillators are widely used in radiation physics due to their beneficial characteristics. Scintillators have a very fast decay time (ns), which results in a very good time resolution (ns to ms scale). Scintillators can be fabricated in any size and shape. They can be made of plastic material which is water-equivalent. There are differences in the scintillation process of organic and inorganic materials. The focus of this work is on organic scintillators.

Scintillation is the emission of light resulting from interaction and absorption of ionizing radiation, which is a property of conjugated and aromatic organic molecules. Briefly, the physical process governing the light emission is due to the electronic structure of the carbon atom. The formation of compounds, specifically hydrocarbons, introduces bonding configurations; each carbon atom forms three sigma bonds with adjacent carbon atoms and a hydrogen atom, and a weak pi bond with another carbon atom. The free-electron model developed by Platt (Platt 1949) treats the pi orbitals as orbitals of free electrons about the perimeter of the molecule. Furthermore the theory includes a pi orbital wave function that is periodic and introduces discrete energy levels for the pi electrons (Birks 1964). When a pi electron de-excites from the first excited energy state to the base energy state it can produce an ultraviolet photons. Then, wave length shifters, in the form of secondary flours, are added to absorb and re-emit the ultraviolet photon to a lower energy photon (visible spectrum). A liquid organic scintillator is a cocktail of primary scintillator material and flours that allow for different properties depending on the application (for example, matching the detector spectral response with the scintillator light emission).

Two seminal papers by Beddar et al. characterized the response of optical fibre coupled plastic scintillators for use in conventional photon and electron radiotherapy (Beddar *et al* 1992c, 1992b, 1992a). Plastic scintillation detectors (PSD) were found to be independent to dose, dose rate and angle of incidence. Furthermore, PSDs were found to be reproducible with high accuracy <1%. The fast decay

rate of scintillators enables PSDs to be used for in-vivo dose measurements and real time measurements.

Earlier prototypes of volumetric scintillator detector demonstrated the potential to measure the dose distribution of spot scanning proton beams (Archambault *et al* 2008, Beddar *et al* 2009). The system was able to measure the range of spot scanning beam very efficiently with sub-millimeter accuracy (Hui *et al* 2015). Robertson *et al* also demonstrated a volumetric scintillator prototype using two orthogonally placed CCD cameras to measure the range and lateral position of the beam (Robertson 2014).

2.6 Ionization quenching

The first theory for scintillation was introduced by Birks in 1951 (Birks 1964). It assumes that a beam of ionizing radiation crossing a scintillator medium will produce a number of “excitons” (excited or ionized molecular structures of organic material) per unit path length proportional to the stopping power of the beam ($A dE/dx$). However, the beam would also produce a given quantity of damaged molecule proportional to the beam stopping power ($B dE/dx$). Thus, the scintillation response per unit length is given by,

$$\frac{dS}{dx} = \frac{A \frac{dE}{dx}}{1 + kB \frac{dE}{dx}} \quad (2.1)$$

where the parameter k describes the quenching resulting from the capture of excitons by the damaged molecule and preventing it from radiative de-excitation. The values A , and kB are found by fitting experimental data with equation 2.1. Extensions to Birks model were investigated to generate better model fits (Beaulieu and Beddar 2016). However, the simple semi-empirical model has little predictive abilities of the scintillation response.

If we maintain the assumption that production of excitons per unit path length is proportional to the energy lost by the ion, the difference in the scintillation for ions of different atomic number

indicates a difference in the energy deposition process of those ions. This difference comes from the difference in the spectrum of secondary electrons. Following this discovery, new ionization quenching models were developed that relate the light production inside a scintillator material to the energy distribution of the ion and the secondary electrons. Many of these models separate the energy deposition surrounding the ion's track in a strongly quenched core and a non-quenched penumbra (Beaulieu and Beddar 2016, Michaelian and Menchaca-Rocha 1994, Hitachi *et al* 1992, Nikjoo *et al* 2006).

Michaelian and Menchaca-Rocha presented a detailed review of quenching models that account for the differences in secondary electron energy (Michaelian and Menchaca-Rocha 1994, Michaelian *et al* 1997). They have also developed an analytical quenching model, the energy deposition by secondary electrons (EDSE) based on impulse approximations. Figure 2.2 demonstrate the radial dose distribution $\rho(r)$ of a proton beam in a generic plastic scintillator (polystyrene) using the EDSE model. In chapter 5, the EDSE model will be further discussed for use with the 3D scintillator detector.

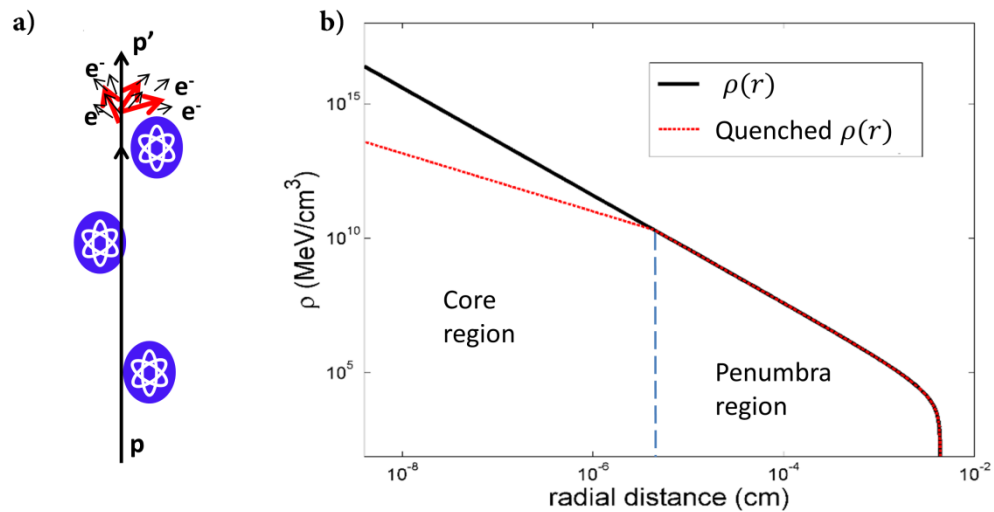


Figure 2.2 a) A schematic of a proton track interacting with matter, resulting in a shower of secondary electrons b) Electron energy deposition density per unit path length of the incident ion beam

(proton 98.6 MeV) as a function of the radial distance from the ion's track (solid line). The EDSE model assumes a region close to the ion's track (core region) where the scintillator quenches (red dotted line).

Chapter 3 : 3D scintillator detector characterization

This chapter is based upon material that was published in Physics in Medicine and Biology in June 2017 by the author of this dissertation [Darne, C. D., Alsanea, F., Robertson, D. G., Sahoo, N., & Beddar, S. (2017). Performance characterization of a 3D liquid scintillation detector for discrete spot scanning proton beam systems. Physics in Medicine & Biology, 62(14), 5652.]. Upon transfer of copyright, IOP Publishing grants back to authors the right to include the article in research theses or dissertations. Portions of this work has been modified to conform to the overall style of this dissertation.

The first and second authors (C.D.D., and F.A.) contributed equally to this work. C.D.D. and F.A. have designed the experimental methods of this research, and performed all experiments. F.A. provided the analysis codes. C.D.D. has designed the system hardware. C.D.D. and F.A. drafted the manuscript. All authors have read and contributed on the manuscript.

© Institute of Physics and Engineering in Medicine. Reproduced with permission. All rights reserved

3.1. Introduction

Even as photons continue to be used for conventional external-beam radiation therapy, the use of proton therapy continues to grow. The steep dose gradients around the Bragg peak for proton beams can be used to develop treatment plans that efficiently target tumors while reducing the exposure to surrounding healthy tissues. In particular, the intensity-modulated proton therapy technique facilitates implementation of three-dimensional (3D) conformal therapy (Kooy and Grassberger 2015). It uses complex radiation fields that vary dynamically in space and time. Spot-scanned or pencil-beam proton therapy is an attractive approach because it can efficiently paint complex tumors in three dimensions, avoid critical organs, and lower the harmful neutron background (Xu *et al* 2008).

However, the developmental pace of clinical dosimeters has lagged behind that of the significant recent technological advances in proton delivery systems. Thus, reliable monitoring of complex beams is challenging with the currently available clinical dosimeters.

The gold-standard for dosimetry, the ionization chambers, in principle, can generate a 3D dose distribution by scanning them through a water phantom. However, in practice, these single-point measurements are time consuming and are therefore poorly suited for mapping complex and dynamic treatment plans. They also suffer from volume averaging, which further impedes their use in high-resolution dose mapping. A two-dimensional (2D) array of ionization chambers (Poppe *et al* 2006) or diodes (Létourneau *et al* 2004) is a good alternative to a single ionization chamber for mapping large-field dose variations and symmetry. However, 2D arrays suffer from relatively poor sampling frequency because of their size, large inter-chamber separations, and are subject to field disturbances caused by their electrical connections (Archambault and Rilling 2016). High water-equivalency for plastic scintillators, in addition to their energy independence, and flexibility in measuring both x-ray and electron radiation fields make them a good fit for precision dosimetry applications (Beddar *et al* 1992b). Thin plastic scintillation sheets have been used for performing high resolution and rapid beam

measurements for 2D photon (Petric *et al* 2006, Collomb-Patton *et al* 2009) and proton dosimetry (Torrise 2000).

3D chemical dosimeters that undergo chemical composition changes upon irradiation, such as Fricke and polymer gels, have been extensively studied (Lepage and Jordan 2010). However, practical difficulties such as preparation time, sensitivity to gel preparation, and loss of spatial information from ion diffusion (in Fricke gels) have limited their use in clinical practice (Schreiner 2015). Commercially available 3D radiochromic gels exhibit little to no diffusion of active species and have been used for commissioning studies of small field systems (Jordan 2010). However, these dose-integrating dosimeters cannot be used for dynamic measurement studies. In addition, they all require a separate dose readout system. Light generation in scintillator depends on the linear energy transfer (LET) of the protons. This LET-dependence causes the detector to under-respond around the Bragg peak and is known as ionization quenching. Quenching must therefore be corrected to obtain accurate dose calculations. While quenching can be precisely corrected for individual proton beams, estimating quenching corrections for 3D chemical dosimeters with intensity integrated signal delivered by multiple beams with variable LETs is not always straight forward (Doran *et al* 2015). Small-volume plastic scintillators are a promising alternative to chemical dosimeters for 3D dosimetry (Kroll *et al* 2013), but need further development to be useful for clinical applications.

Therefore, volumetric or 3D detectors that can measure both large and small fields and overcome the dosimetric shortcomings of existing 3D dosimeters are urgently needed. Early work with volumetric liquid scintillation detectors for 3D dosimetry showed that these detectors have several promising features (Beddar *et al* 2009). First, they are tissue- or water-equivalent, enabling dose detection with minimal field perturbation (Ingram *et al* 2015). Second, they have high spatial resolution (Archambault *et al* 2012). Third, they exhibit good temporal resolution, with nanosecond scintillation-response time and detection time in the range of milliseconds. This high temporal resolution allows

quenching correction for individual scanning beamlets. Thus, accurate determination of the total dose delivered by a treatment plan is now possible. Fourth, they are flexible for applications involving photons, protons, and other heavy-ion particles.

Earlier work by the author's group has focused on the development of a large volume of liquid scintillator coupled to optical camera detectors for 2D dosimetry of photons (Pönisch *et al* 2009) and proton beams (Beddar *et al* 2009, Archambault *et al* 2012, Hui *et al* 2015). In the work described here, we describe the design and development of a new 3D detection system based upon liquid scintillation. We then discuss the characterization methods used for validating the detector's performance for proton therapy.

3.2. Methods and materials

3.2.1. Design of the 3D detection system

Figure 3.1(a) depicts the 3D liquid scintillator detector system and setup. The scintillation volume consisted of a $20 \times 20 \times 20 \text{ cm}^3$ liquid scintillator-filled tank. This scintillation volume was constructed from a combination of clear and opaque acrylic (density 1.18 g cm^{-3}) with a wall thickness of 11.6 mm. The entire volume was securely sealed to prevent leakage of the liquid scintillator. Figure 3.1(b) shows typical integrated scintillation light profiles of a proton beam captured by the three cameras.

The reference coordinate system was oriented as shown in figure 3.2(a). Cameras X, Y, and Z image the x-, y-, and z- projection images from the scintillation volume, respectively. As illustrated in figure 3.2, camera X was positioned such that it pointed directly into the front surface of the tank perpendicular to the proton beam direction (the z-axis). For this work, we considered the center of the scintillation volume as the origin point. The beam was incident on the left surface of the scintillation volume and traveled through the origin point along the z-direction. Additional beam profiles were captured using two mirrors oriented at an angle of 45° to the top and right surfaces of the scintillation volume. These mirrors redirected the scintillation photons to cameras Y and Z. Thus, cameras X and Y

captured depth profiles of the beam while camera Z captured a beam's-eye view without directly exposing the camera sensor to ionizing radiation. Thus, three mutually orthogonal perspectives of the scintillation light were captured.

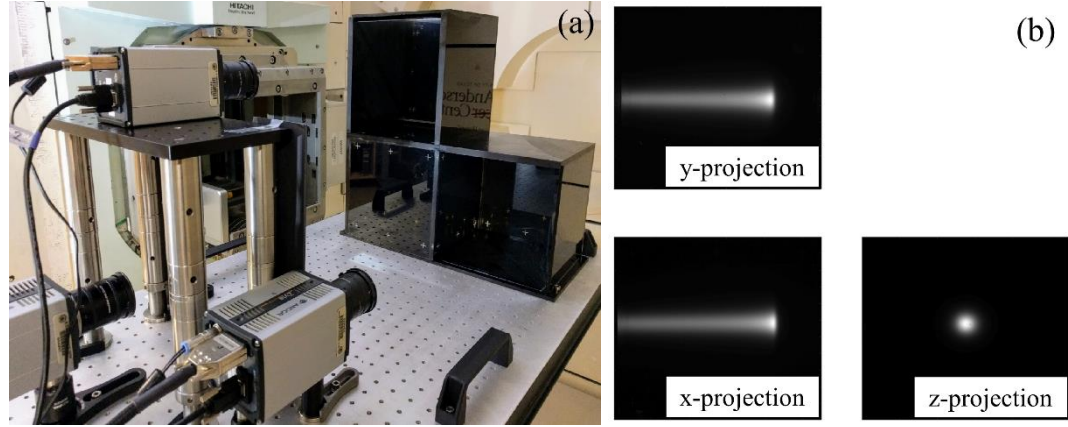


Figure 3.1 (a) Photograph of the 3D liquid scintillator detector setup placed on a patient couch in a discrete spot scanning proton beam gantry. **(b)** Integrated light profiles of a proton beam captured using the three-camera setup.

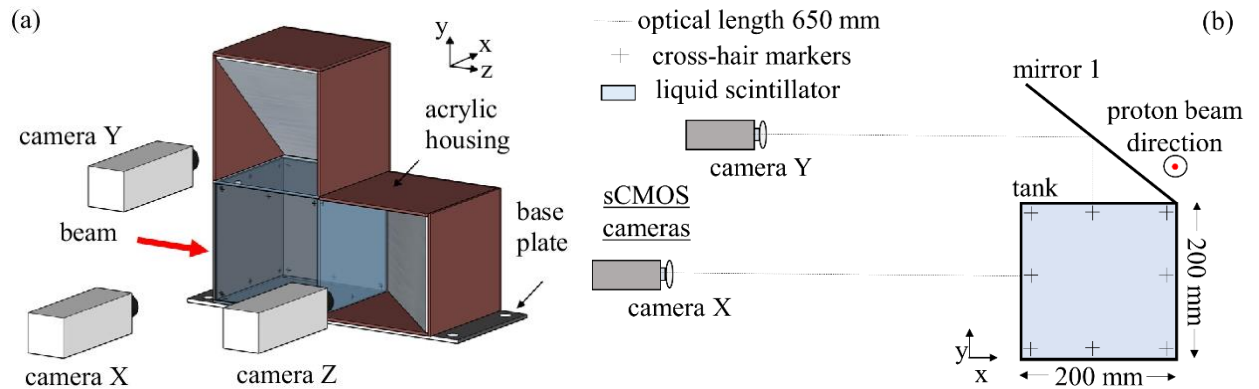


Figure 3.2 Schematic of the 3D liquid scintillation detector. **(a)** 3D model of the system. **(b)** Right-side view of the detector system with cameras X and Y imaging the scintillation volume. A 45° mirror mounted on the top of the volume redirected scintillation light to camera Y. Camera Z and side mirror are not shown in the 2D schematic for simplicity.

The liquid scintillator-filled volume and the two mirrors were housed in an opaque acrylic housing to reduce light leakage and for providing mechanical stability to the structure. Finally, a base-plate was used to securely mount the scintillator volume and the mirror assembly on an optical board.

Eight cross-hair markers with known geometries and relative positions were equidistantly placed on the inner sides of each tank surface. These built-in calibration markers were a big improvement over the earlier prototype, which required laborious acquisition of multiple images of a ruler inside the volume. A previously developed geometric calibration technique (Hui *et al* 2015), made use of these cross-hair markers to determine the optical length from the surface of the scintillation volume to the camera sensor plane, angular shift, and translational shift of the volume relative to the camera. The optical length and angular shift were determined by minimizing the square difference between the measured and calculated distances for multiple pairs of cross-hair markers. Likewise, pixel locations of the markers from the front and back surfaces of the volume along with the angular shift were used for calculating the translational shift of the camera center with respect to the center of the volume. Based on the calibration process, identical optical lengths were set for all the cameras (650 mm).

OptiPhase HiSafe 3 (PerkinElmer, Waltham, MA) was used as the liquid scintillator for this study. This liquid scintillator, with a density of 0.963 g cm^{-3} , serves as both a phantom and a detector medium (Ingram *et al* 2015). The peak emission wavelength of the scintillator is around 420 nm with a decay time of 1.4 ns and quantum yield of 0.83.

Finally, the system was mounted on an optical board ($1200 \times 600 \times 58 \text{ mm}$) that secured the relative orientation of the components, making the system robust and portable. The rigid optical setup also ensured that the optical calibration would not change accidentally while transporting the system or during daily operation.

3.2.2. Optical system design

Three identical Zyla 5.5 scientific complementary metal oxide semiconductor (sCMOS) cameras were used in this work (Andor Technology Ltd., Belfast, UK). sCMOS offers relatively lower read noise (<2.9 e⁻ root mean square at the fastest pixel readout speed, 560 MHz), better resolution, and wider dynamic range over interline charge-coupled device technology that was previously used for earlier detector prototypes. The sCMOS cameras were each equipped with a 5.5-megapixel sensor (2560 × 2160 pixels) with an individual pixel size of 6.5 μm. They supported a full-frame transfer speed of 30 frames per second (fps) using a 16-bit data range. The imaging sensors were thermoelectrically cooled to 0° C to suppress dark current. The cameras were fitted with identical fixed focal length objective lenses.

3.2.3. Optical artefact corrections

Before the three cameras can be used for scintillation detection, optical artefacts associated with each camera were individually tested and corrected (Robertson *et al* 2014). This involved setting similar optical settings, including lens focus and aperture, and identical optical lengths. Corrections for refraction at the air-liquid scintillator interface and changes in image perspective with distance were implemented. Lens distortion was corrected using the Camera Calibration Toolbox for MATLAB (Bouguet 2010). The three lenses demonstrated a mean distortion of 0.22 pixels along the radial distance, and their focal lengths matched within 0.2%.

The background signal contributed by ambient light, dark current, and camera read noise was also taken into account. To ensure that the cameras had similar dark current and read noise levels, image acquisitions commenced after the cameras reached a stable operating temperature of 0 °C. The background signals for the three cameras were within 1% of each other for camera integration times varying from 10 ms to 1 s. A spatial median filter was applied to the 3 × 3 region surrounding each pixel for eliminating the influence of stray radiations on the sensors.

Because all three cameras demonstrated matching characteristics, only the performance characteristics of the camera X are described here. All experiments were performed using the discrete spot scanning proton beam gantry at the MD Anderson Proton Therapy Center. As shown in figure 3.1, the 3D detection system was placed on the patient couch such that the beam isocenter aligned with the left surface of the scintillation volume. The gantry angle was set to 270°. All image computations and analyses were performed using MATLAB (version R2014b; MathWorks, Natick, MA).

3.2.4. Spatial resolution

One of the advantages of using volumetric detectors is their ability to capture dose distributions with high spatial resolution. The resolution limit depends on several aspects of the optical system design, including sensor size, individual pixel size, choice of objective lens, distance of the imaging plane from sensor, and optical artefacts. To produce a sharp image, objective lenses for volumetric imaging must be able to maintain good focus over the entire depth of the scintillation volume. The distance over which the lens can retain reasonably good focus is referred to as the depth of field. Therefore, the lens selection was based on calculations of depth of field (Beddar *et al* 2009). Using a 20.5 mm fixed focal length objective lens (Schneider Optics, Van Nuys, CA) with an f/8 aperture and a working distance of 650 mm, a 205 mm depth of field was obtained. These settings resulted in a field of view that was larger than that required to image the 20 cm² area of the scintillation volume face. We therefore chose a smaller region of interest (1100 × 1100 pixels). Furthermore, spatial resolution changes as a function of the object's distance from the lens. It is important to accurately quantify this change in spatial resolution through the entire scintillation volume depth, especially for 3D dose reconstruction.

3.2.5. Camera linearity

For quantitative imaging, the camera is expected to demonstrate a linear response so that a simple yet accurate conversion of the detected light to the deposited dose is possible. To verify the camera's linearity, the intensity counts at the peak of the light profile for six doses ranging from an average of 0.1

Gy–12 Gy were recorded. These doses were delivered three times for each of five proton beam energies: 161.6 MeV, 144.9 MeV, 124 MeV, 100.9 MeV, and 85.6 MeV. We also calculated a non-linearity factor describing the deviation in camera counts at each dose level from the corresponding linear regression fit. Additionally, the signal-to-noise ratio (SNR) was calculated for individual pixels over an area of 21×21 pixels around the peak light intensity profile, where the majority of the proton dose is deposited. The SNR was calculated using the equation, $20 \times \log\left(\frac{\text{signal}-\text{background}}{\sigma_{\text{background}}}\right)$, where σ is the standard deviation in the background signal.

3.2.6. Camera stability

Another important performance characteristic for the detector is the ability to maintain a stable light output for a given dose input over a period of time. To assess the camera stability, a proton beam with an energy of 161.6 MeV and a dose of 1.16 Gy was delivered to the detector 10 times over a single imaging session. The experiment was then repeated over three sessions spanning a week. Stability is defined using the equation $\frac{\sigma_{\text{signal}}}{\langle \text{signal} \rangle}$, where σ_{signal} indicates the standard deviation for an individual pixel intensity while $\langle \text{signal} \rangle$ is the average intensity for that pixel over three sets of measurements. An area of 21×21 pixels around the maximum signal intensity was then selected and stability was assessed for all the individual pixels in that area. The reported stability for the system is the mean stability over the entire area.

3.2.7. Proton range measurement accuracy

The detector's proton range measurement accuracy was assessed for all 94 proton energies generated by the synchrotron, ranging from 72.5 MeV to 221.8 MeV. The measurements were divided in two batches: low-energy batch consisted of energies ranging from 72.5 MeV to 141.6 MeV with a mean proton range less than 20 cm; high-energy batch delivered energies from 129.2 MeV to 221.8 MeV with a mean proton range exceeding 20 cm. To ensure that the Bragg peaks from the high-energy batch were restricted to the scintillator medium, a plastic water buildup with a water-equivalent thickness of

105 mm was placed in the beam path. An average dose of 0.25 Gy was delivered on the central beam axis for each beam energy and all the energy deliveries were repeated nine times. To determine the beam range, pixels of the captured scintillation image were vertically summed to generate a one-dimensional (1D) integrated light profile along the z-axis. At the MD Anderson Proton Therapy Center, the proton range is defined as 90% integral depth dose distal to the Bragg peak (Gillin *et al* 2010). Based on a recent study, we found that the distal 90% of the light peak provides the most accurate range measurements without correcting for quenching (Hui *et al* 2015).

Since this study involved range measurements in a liquid scintillator; therefore, the range measured in the scintillator medium was first converted to the water-equivalent range by accounting for the ratio of the stopping power of water to that of the liquid scintillator. This stopping-power ratio was experimentally found to be 0.995 by measuring the range of a 161.6 MeV beam with varying thickness of water-equivalent build up material placed in the beam path (Hui *et al* 2015, Archambault *et al* 2012). Ionization chamber measurements collected as part of the beam commissioning studies served as the reference measurements. For clinical applications, the detector must be able to detect the smallest dose fractions delivered in treatment plans. At these small dose fractions, the influence of noise on range measurement accuracy is expected to increase. The minimum deliverable spot MUs from the synchrotron at The University of Texas MD Anderson Cancer Center Proton Therapy Center are 0.005. Considering the dose at the Bragg peak to be about 0.25 Gy MU⁻¹ (for 72.5 MeV) to 1 Gy MU⁻¹ (for 221.8 MeV), the minimum dose a spot can deliver at the Bragg peak is in the range of 0.13 cGy–0.5 cGy. Therefore, to determine the impact of noise on range-measurement accuracy at very low delivered doses, the beam ranges were measured as a function of beam dose for three separate energies (161.6 MeV, 144.9 MeV, and 124 MeV), with the beam intensities varying over average doses of 0.87 cGy–1.16 Gy.

3.2.8. Lateral beam profiles

Lateral beam profiles can be used for determining the size of individual beam spots that vary with the proton energy. In this study, we used the beam images captured by camera X to plot lateral 1D integrated light profiles perpendicular to the beam axis. For the 161.6 MeV proton beam energy, these 1D lateral profiles were plotted at two different depths within the scintillation volume: $z = 20$ mm and $z = 166$ mm. The normalized integrated 1D light profiles were compared with the normalized dose profile of the proton beam as determined using a validated Monte Carlo (MC) radiation transport code MCNPX, version 2.7d (Sawakuchi *et al* 2010). The full width half maximum (FWHM) for these 1D profiles was selected as the quantification parameter. Lateral light profiles for off axis beams that were displaced ± 4 cm and ± 8 cm along the y-axis, were plotted at $z = 20$ mm and compared with the lateral profile of the beam on the central axis.

The measured lateral beam profile of the 161.6 MeV beam was compared to the Monte Carlo simulation to determine an analytical point spread function (PSF) of the system. The PSF was a linear combination of a 2D Lorentzian function and a 2D Gaussian function with a constant weighting factor. The parameters of the PSF were determined iteratively by comparing the deconvolved measured lateral beam profile to the simulated lateral beam profile of a 161.6 MeV beam. The PSF was used to deconvolve four selected proton beam energies (161.6 MeV, 144.9 MeV, 100.9 MeV, and 85.6 MeV) to the applicability of this PSF.

3.2.9. Determining 3D beam locations

The unique benefit of employing multiple imaging cameras is that combining 2D images from different cameras produces accurate location of the 3D proton beam anywhere inside the tank. Here, we used the cameras Z and X to locate the beam position in the z and x projection images, respectively. A beam with an energy of 161.6 MeV was selected. The beam was initially positioned on the central beam axis and then displaced 4 cm off-axis along both directions of the x-axis. Similar beam translations

were then repeated along both directions of the y-axis. A dose of 0.28 Gy was delivered three times at each location.

3.3. Results

Figure 3.3 shows 1D integrated light profiles generated for five beam energies. Depending on the dose magnitude, each proton beam was delivered and captured for durations ranging from 11 ms to 4 s.

Figure 3.2(a) shows the normalized depth light profiles for five beam energies imaged using camera X.

The higher-energy profiles show wider Bragg peaks caused by greater energy straggling. Similarly, figure 3.3(b) shows the normalized lateral profiles of the proton beams at the same five energies obtained using camera X. As expected, proton beams with lower energies had a wider lateral profile.

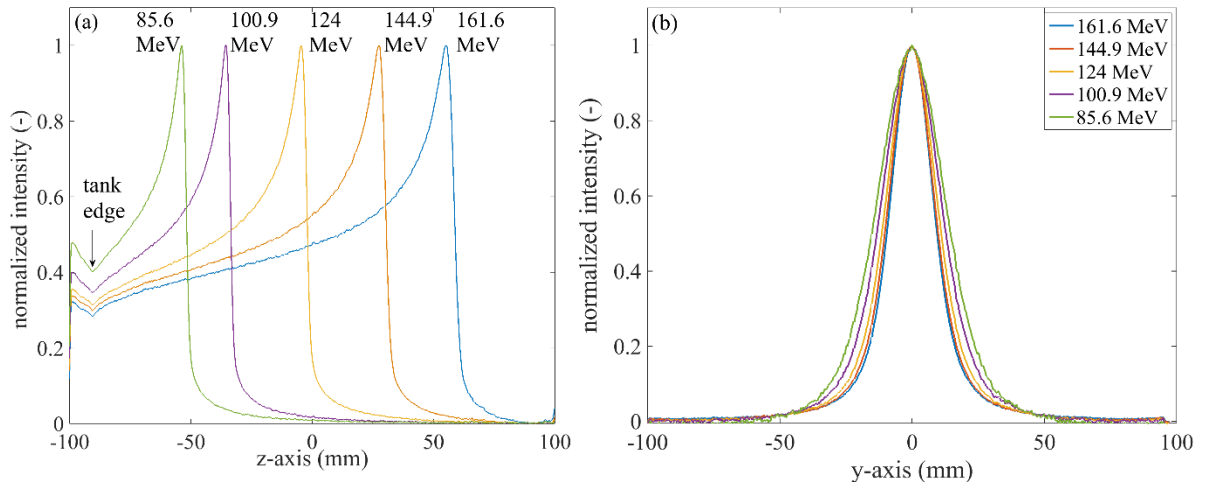


Figure 3.3 (a) Normalized depth scintillation light profiles for five beam energies measured with camera X. **(b)** Normalized lateral scintillation light profiles of the same beam energies. On both figures, the x-axis shows the location of the Bragg peak with respect to the center of the tank volume.

3.3.1. Spatial resolution

As shown in figure 3.4, the detector demonstrated good spatial resolution that varied linearly from the front (65 cm from the sensor plane) to the back (85 cm from the sensor) of the scintillation volume, with a mean resolution of 0.208 mm. This sub-millimeter resolution can be used for generating detailed

light distribution profiles and is a clear improvement over that of the currently used detectors for clinical proton beam dosimetry.

3.3.2. Camera linearity

The recorded light intensity from camera X increased as a function of increasing dose, as shown in figure 3.5(a) for the 161.6 MeV beam energy. A non-linearity parameter calculated for the camera was 0.39% over five separate energies, indicating that the camera had an excellent linear response over a three-order-of-magnitude change in delivered dose. The SNR varied linearly from 20 dB to 85.5 dB over a dose range of 5.3 mGy–10.6 Gy. The lowest dose that can be delivered by our synchrotron at 161.6 MeV is 2.9 mGy; therefore, the detector was able to detect proton beams just above this lowest dose (figure 3.5(b)).

3.3.3. Camera stability

The average stability of the detector was 1.08% over 3 weeks, with week-to-week variation of 0.04%. These results indicated that the camera had an excellent, stable response to the delivered dose.

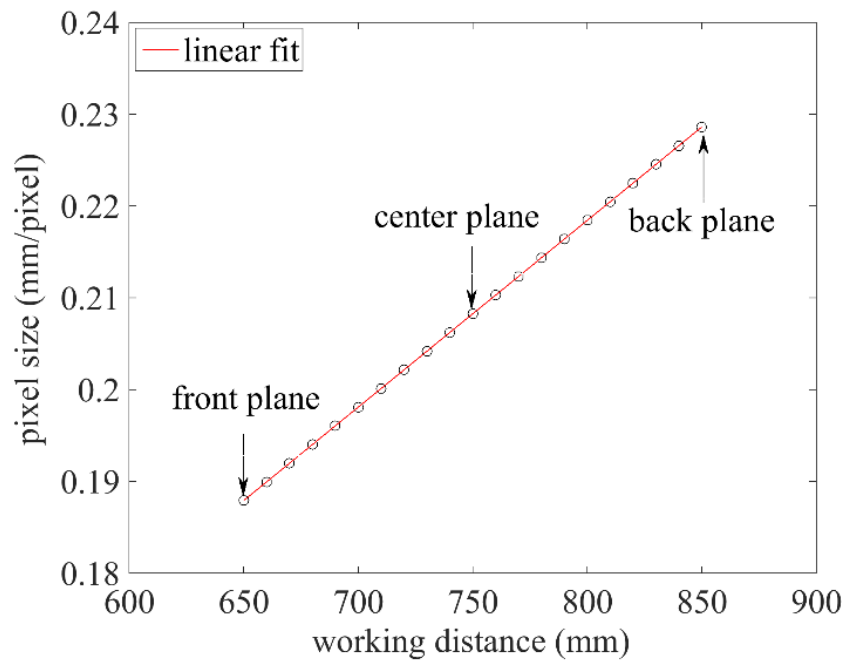


Figure 3.4 Spatial resolution of the detection system as a function of working distance from the camera sensor plane to different imaging planes within the scintillation volume. The change in resolution was modeled using a linear fit.

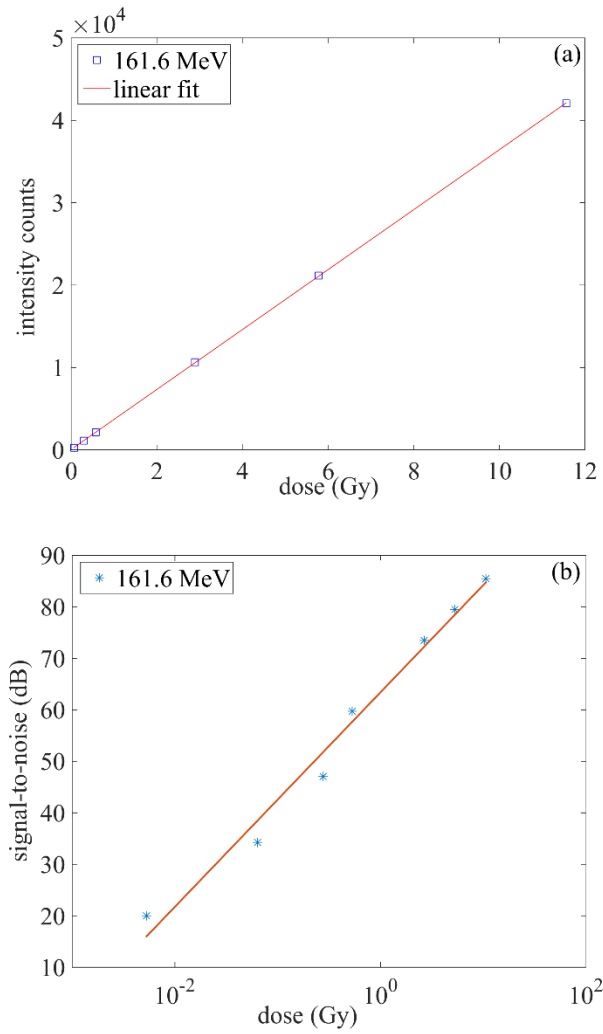


Figure 3.5 (a) Linear response of the camera to increasing dose for 161.6 MeV beam energy. **(b)**

Signal-to-noise of camera X as a function of the delivered dose (Gy).

3.3.4. Proton range measurement accuracy

Figure 3.6(a) shows the proton-beam range-measurement accuracy plotted as a function of the beam locations inside the scintillation volume measured using camera X. The range-measurement accuracy is calculated as the difference between the measured and reference beam ranges, which is shown for all 94 synchrotron-generated energies. After linear fitting, the average measurement accuracy over 94 energies was -0.07 ± 0.03 mm.

Relatively larger errors (still within 1 mm) in range measurements were observed for the proton beams with Bragg peaks located towards the right and left edges of the scintillation volume. We attributed this effect to beam reflections from the inner surfaces of the scintillation volume. To confirm that this was the case, five discrete energies from 211.6 MeV to 221.8 MeV with Bragg peaks located near the scintillation volume edge were delivered. The same energy beam deliveries were then repeated while attenuating their ranges using a water-equivalent phantom in the proton path, so that the Bragg peaks were shifted away from the volume edge. The range measurement errors were 0.78 mm when the Bragg peaks were located near the edges and 0.14 mm away from the edges. This confirmed that internal beam reflections are a source of error in range verification studies. Therefore, Bragg peaks of beams must be located away from the edges of the scintillator volume during range measurements.

We also assessed the impact of low-dose deliveries on proton-beam range measurement accuracy over three different energies using six dose levels. Whereas the difference in measured range was within ± 0.2 mm of the reference range, reducing dose levels increased the uncertainty in the range measurements. As shown in figure 3.6(b), for a beam energy of 161.6 MeV, the uncertainty increased from ± 0.006 mm to ± 0.701 mm when the delivered dose was reduced from 1.16 Gy to 0.87 cGy. Despite this increase, the overall uncertainty was less than 1 mm. The average increase in uncertainty over all three energies for the highest and lowest doses were ± 0.01 mm at 1.16 Gy and ± 0.355 mm at 0.87 cGy. These results illustrated that this detector is capable of accurate beam-range measurements even for extremely low doses.

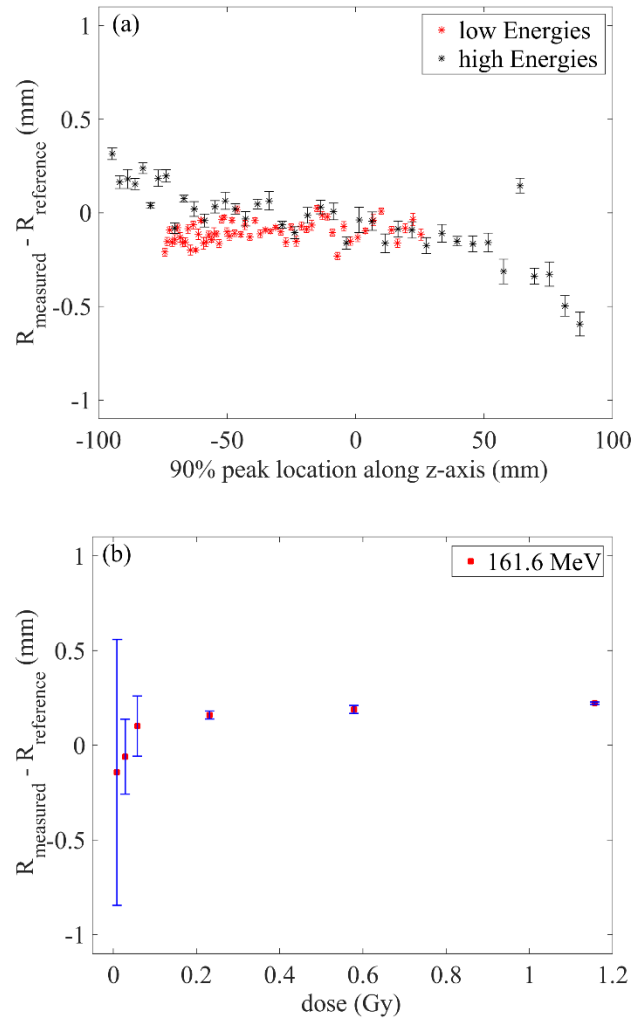


Figure 3.6 (a) Proton-beam range-measurement accuracy plotted for all 94 energies delivered by the synchrotron. The difference between the measured (R_{measured}) and reference ($R_{\text{reference}}$) beam ranges is plotted as a function of their range inside the tank volume. The energies were delivered in two batches: low-energy (72.5-141.6 MeV) and high-energy (129.2-221.8 MeV). **(b)** Uncertainty in range measurements for low-dose deliveries. Uncertainty in measurements is represented by the error bars in both the figures.

3.3.5. Lateral beam profiles

The FWHM of lateral beam profiles was used for calculating the beam spot sizes. Figure 3.7(a) shows the normalized integrated 1D lateral light profile at a depth of $z = 20$ mm inside the scintillation volume along with a profile obtained from Monte Carlo simulation at the same depth. The FWHM of the lateral

profile at $z = 20$ mm depth along the beam axis was 1.6 mm (9.5%) wider than that of the Monte Carlo simulation. The FWHM of the lateral profile at depth $z = 166$ mm (not shown) was 2.2 mm (10.6%) greater than that of the Monte Carlo simulations. The photon travel paths for both profiles from the location of scintillation generation within the tank volume to camera X were approximately the same; therefore, we observed a similar widening of the measured profiles.

Lateral 1D light profiles measured at $y = \pm 4$ cm and $y = \pm 8$ cm from the central beam axis at a depth of $z = 20$ mm are shown in figure 3.7(b). The lateral light profile along the central beam axis ($y = 0$ cm) was used as the reference. The FWHMs of the off-axis spots were 2.6% (at -4 cm), 4.6% (at -8 cm), 2.6% (at 4 cm), 2.5% (at 8 cm) wider than that of the single energy spots located along the central axis. This broadening of the off-axis beam profiles can be accounted for in the future by correcting them for the vertical angle they subtend with respect to the central beam axis. Thus, practically identical lateral light profiles can be obtained away from the central beam axis for a given depth.

Figure 3.3(a) shows depth scintillation light profiles with tails towards their distal ends. Such tails were not present in the depth dose profiles measured using ionization chamber. Further, lateral integrated light profiles (refer figure 3.7(a)) were relatively wider compared to those obtained through Monte Carlo simulations. These differences could be attributed to image blurring from photon scatter inside the scintillation liquid as well as from imperfections in the lens optics. Robertson et al (2014) has shown that both these artefacts can be accounted for by determining and later deconvolving the acquired proton beam images with point spread function for the system. In this work, an analytically determined point spread function of the optical system was applied to four proton beam energies. Figure 3.8 shows the match between the MC lateral profile and the deconvolved measured lateral profiles at the Bragg peak depth.

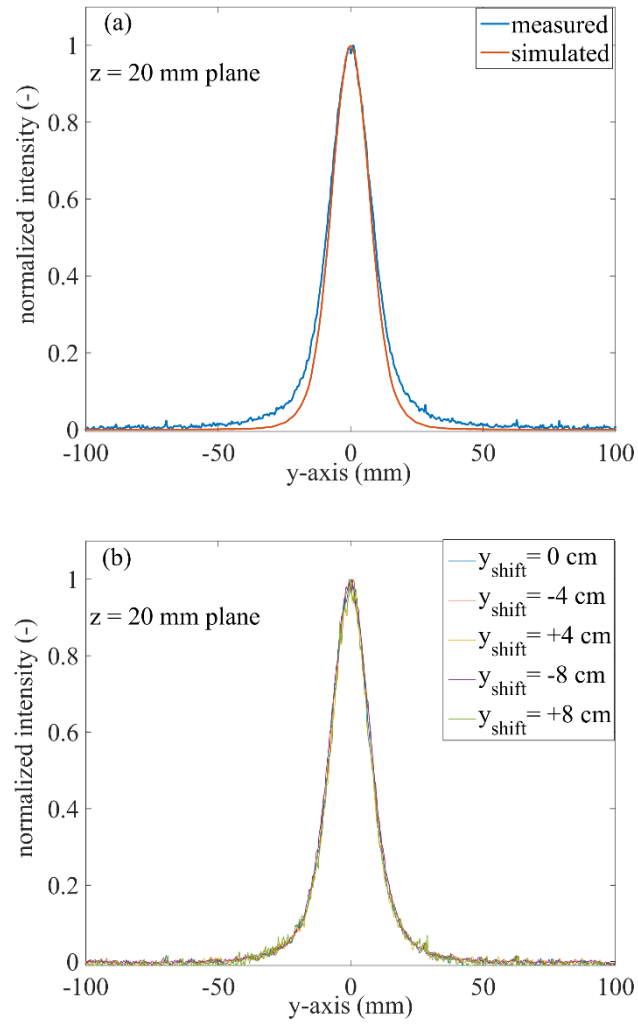


Figure 3.7 (a) Lateral 1D integrated light profile recorded by camera X is compared to Monte Carlo simulation of lateral dose profile at depth $z = 20$ mm from the entrance of the scintillation volume. **(b)** Lateral 1D integrated light profiles of spots of single beam energies incident at different locations from the central axis ($y_{\text{shift}} = 0$ cm) along the y-axis ($y_{\text{shift}} = \pm 4$ cm and ± 8 cm) are shown.

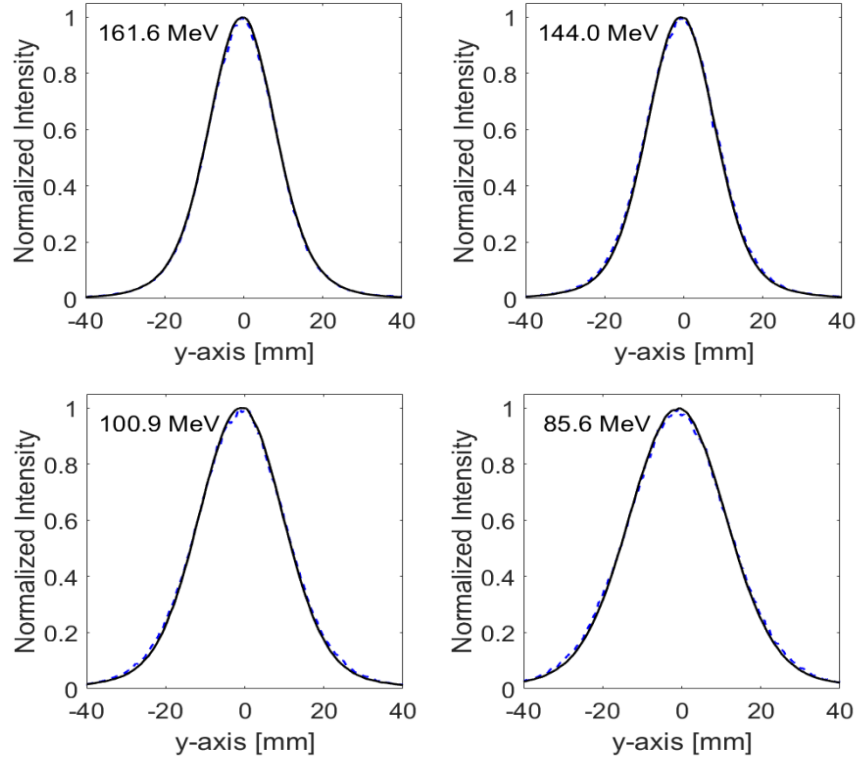


Figure 3.8 Lateral 1D deconvolved integrated light profile recorded by camera X (dashed line) is compared to Monte Carlo simulation (solid line) of lateral dose profile at Bragg peak for 161.1 MeV, 144.0 MeV, 100.9 MeV, and 85.6 MeV.

3.3.6. 3D beam locations

The location of a beam in three dimensions can be determined by combining the 2D views of a proton spot from multiple cameras. We used the cameras X and Z to record the 2D beam profile in the x- and z-projections images, respectively. The geometric calibration algorithm then accurately mapped the physical location of these spots from their recorded pixel locations. The nominal beam locations programmed into the beam delivery system and the measured 3D locations are compared in figure 3.8. Figures 3.9(a) and (b) show the beam location accuracy in the z- and x-projections, respectively. We observed a location accuracy of 0.3 mm in the x-projection but an accuracy of 2 mm along the lateral z-projection. Lower accuracy in the z-projection could be attributed to a combination of errors such as beam positioning by the steering magnets and imperfect detector calibrations. Further, in this work,

the location accuracy was assessed by comparing the measured beam locations to the nominal or programmed beam locations. Greater location accuracy is expected by comparing the measured locations to the actual delivery locations as recorded by the spot position monitor.

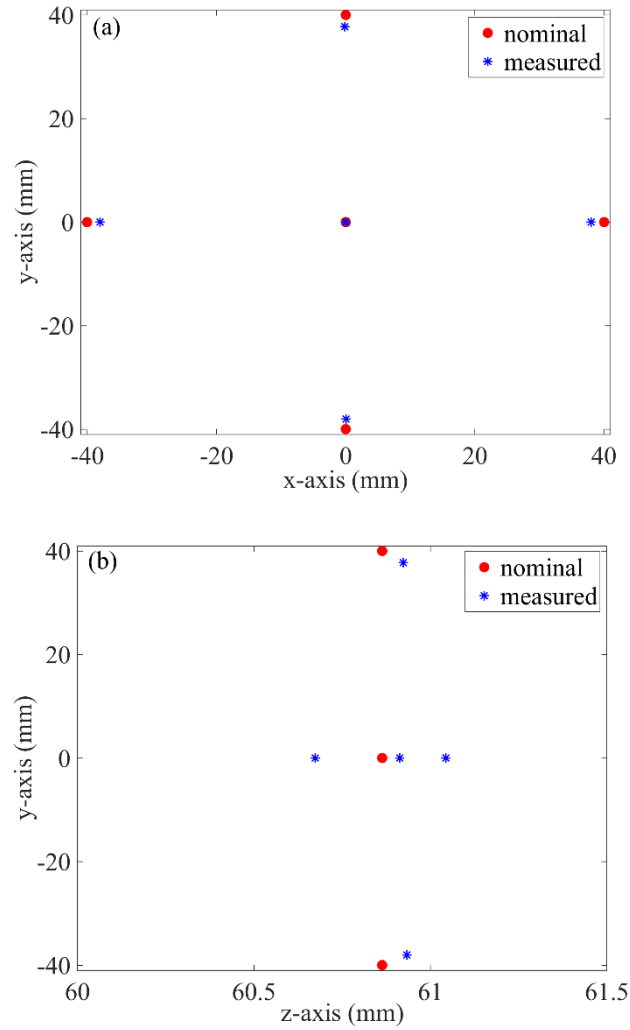


Figure 3.9 Spot location accuracy calculated as the difference between measured and programmed beam locations inside the scintillation volume is plotted for a beam energy of 161.6-MeV (nominal location of 60.85 mm within the scintillation volume) and for the beam locations, (0,0), (± 4 cm,0), (0, ± 4 cm), in the **(a)** z-projection, and **(b)** x-projection.

3.4. Discussion

This study demonstrated that a liquid scintillator-based detector can be used with multiple orthogonally placed cameras to sample large-area ($20 \times 20 \text{ cm}^2$) proton-therapy fields in three dimensions. Because the liquid scintillator is water-equivalent, measurements can be performed under pristine beam conditions, with minimal alteration to the proton fluence. The detector also generated high spatial resolution (0.2 mm) light distribution profiles.

The detector is uniquely suited for dynamic imaging of discrete proton spots because it can perform rapid imaging of the proton beams with high temporal resolution (11 ms). Moreover, the temporal resolution could be further improved for use in quality assurance studies where the placement of the beam path is predetermined, for example, in beam range validations. Using a smaller region of interest tightly encompassing the beam would produce faster image acquisition rates for such studies.

We found that all three cameras used for 2D detection of the proton beams displayed good stability and dose linearity. Good camera stability indicates that no correction or additional compensation factors were necessary to correct for systemic drift or camera output change over time when measuring a given beam condition. We also tested the cameras for their ability to linearly capture scintillation light for doses up to 12 Gy. Camera response linearity allows for meaningful interpretation of captured light to dose and is critical for dosimetry. For camera Z that captured the beam's-eye view, camera saturation was reached earlier because of light integration in the beam direction. Thus, most hypo-fractionated treatments (<8 Gy) can be imaged with these cameras. One approach to avoiding camera saturation is by programming the beam deliveries such that the intended large dose is split into multiple synchrotron spills. Refer to figure 4.3 for timing chart on proton delivery by synchrotron. This way the camera can collect signal from each spill, read out the integrated signal, and be ready for the next signal acquisition from the succeeding spill.

3.5. Conclusion

In this work, we designed and developed a 3D liquid scintillator-based detector to rapidly acquire and accurately assess beam characteristics for discrete spot scanning proton beam systems. Highlights of the system capabilities include its high spatial (0.21 mm) resolution and its large 3D volume that can cover most treatment plans (20 cm³). It requires virtually no preparation time after a one-time optical calibration, can be quickly reused, is portable and durable, and provides real-time or near real-time dosimetry data. The key design features of this detector include (a) its three-camera setup, which will support future 3D dose verification methods; (b) its single-board setup with fixed optical equipment to preserve optical calibration and make the system more rugged and portable; and (c) its use of embedded imaging markers for rapid calibration.

In this study, we identified and analyzed several performance criteria for the 3D detector. First good camera performance parameters such as spatial resolution, stability (1%), SNR (20 dB at 0.5 cGy), and dose response linearity (99.6%) were found. Second, the detector was found to be suitable for rapid and accurate beam range verifications for several proton beam energies with an average error of -0.07 ± 0.03 mm. Third, the detector enabled accurate determination of spot beam sizes for all energies. Fourth, the detector facilitated 3D location of the beam position within the detector with good accuracy.

Chapter 4 : Spot scanning camera synchronization

4.1. Introduction

The beams used in proton therapy have a finite range and sharp dose drop-off that allow dose distributions to be highly localized. One method of delivering a conformal treatment plan is by using spot scanning proton therapy. Spot scanning proton therapy involves small bursts of doses known as “spots” that are rapidly scanned across the treatment volume. These individual spots can be used to build and deliver highly complex treatment plans, as in intensity-modulated proton therapy (IMPT). However, the complexity and dynamism of spot scanning proton treatment plans pose a challenge for accurate and efficient dose verification and quality assurance.

In several studies, scintillator-based detectors have been used with an optical camera for fast real-time imaging of scanned pencil proton beams (Beddar *et al* 2009, Archambault *et al* 2012, Hui *et al* 2015, Russo *et al* 2017, Almurayshid *et al* 2017). However, in these studies, the camera exposure time and the intervals between images were not coordinated with the pulses from the beam delivery system. This timing mismatch, along with the time needed by the camera to read, digitize, and transfer the recorded charge, referred to as the camera readout cycle, makes the camera unavailable to record the next proton spot. This causes the camera to ignore multiple spot deliveries and can eventually result in poor dosimetric estimation by the detector system. For rapid imaging applications, in which imaging times may be shorter than or comparable to the camera readout phase, the peak camera imaging rate is severely constrained by the camera readout cycle.

Proton spots can have dynamic delivery times that closely match camera readout intervals. One solution to problems resulting from camera readout is to increase the camera exposure time relative to the time required to image a single spot. This reduces the number of times the camera enters the readout phase and simultaneously prolongs the camera exposure, capturing several spots in a single frame. The overall percentage of the spots missed by the camera thus decreases. However, because the camera is not synchronized with the beam, it still fails to capture all the spots in a treatment plan.

Additionally, analysis of the images, for instance proton range calculations, can become complicated owing to the superimposition of multiple spots with potentially different energies and locations in a single image (Hui *et al* 2014). Finally, to ensure imaging of most of the delivered spots, the camera is required to start imaging before the start of beam deliveries and maintain continuous imaging at its maximum operating frequency. This generates large imaging datasets that can be logistically difficult to store and process.

A “spill-based” camera synchronization technique that uses synchrotron-generated signals to trigger and terminate camera cycles has been demonstrated previously (Darne *et al* 2017). While the synchrotron produces a range of proton energies (72.5 - 221.8 MeV), each energy is delivered in a different “spill” of protons, and each spill can contain more than one spot. This imaging approach combines all spots with identical energies into a single spill, which can last up to 4.4 s, in a camera frame. A 2.1-s inter-spill duration allows the camera sufficient time to read and digitize the frame and get ready for the next spill. This synchronized imaging approach can capture all the delivered spots in a flexible manner and uses significantly fewer camera frames (# frames = # spills), which are easier to process. However, superposition of multiple spots at potentially different locations into a single frame can significantly complicate image analysis. In this work, we aimed to improve on the spill-based triggering technique and achieve greater flexibility in synchronizing optical camera images with the beam delivery system by incorporating additional electronics and selecting synchrotron signals that monitor each spot delivery.

4.2. Methods

4.2.1. Proton beam system

The proton beam delivery system at MD Anderson Proton Therapy Center at Houston can generate up to 94 discrete proton beam energies from 72.5 to 221.8 MeV. Each energy is extracted individually in a spill with a maximum spill time of 4.4 s. The synchrotron beam acceleration and deceleration phase

requires around 1 s. The time between each spill is approximately 2.1 s. Each spill can contain multiple proton spots delivered at different locations. These proton spots are extracted out of their orbit in the synchrotron using a radio frequency (RF) kicker. The RF signal duration depends on the charge collected by the dose monitor (DM). The DM is an ionization chamber that collects the charge which corresponds to monitor units (MU). The MU is defined arbitrarily by the International Atomic Energy Agency TRS 398 protocol (Pedroni *et al* 2000), which dictates the amount of charge for an MU. The DM ionization chamber generates a pulse (~ 10 kHz) after collecting 2×10^{-12} C (2 pC). At our proton center, 1 MU is calibrated for a total of 10,000 DM pulses (Gillin *et al* 2010). The MU for each spot can span from a minimum of 0.005 MU to a maximum of 0.04 MU (Gillin *et al* 2010, Zhu *et al* 2010).

The spot can be delivered over a duration of 1 to 10 ms (typical delivery time is 4 ms for 0.04 MU) depending on the dose delivered (Gillin *et al* 2010). A time of 3 ms is required by the proton delivery system to calculate and change the magnetic field strength of the scanning magnets to the next location (Gillin *et al* 2010). A treatment plan can consist of any combination of beam energies, number of spots, and dose delivered for each spot (MU/spot), which consequently affects the delivery time. Thus, the image acquisition times for the camera frames needed to be actively modified for each spot in accordance with the treatment plan. Detailed explanations of the proton therapy system at The University of Texas MD Anderson Cancer Center have been described by Gillin *et al.*, and Smith *et al.* (Gillin *et al* 2010, Smith *et al* 2009).

4.2.2. Cameras

The 3D scintillator detector system used in this study has been explained in detail by Darne *et al.* (Darne *et al* 2017). It consisted of 3 identical Zyla 5.5 scientific complementary metal-oxide-semiconductor (sCMOS) cameras (Andor Technology Ltd., Belfast, UK), and a scintillator tank ($20 \times 20 \times 20$ cm³). Each camera views a different projection of the tank (e.g. Camera X views a projection along the x axis, as shown in figure 3.1 and 3.2). The sCMOS cameras were equipped with 5.5-megapixel sensors ($2560 \times$

2160 pixels) with a pixel size of 6.5 μm . They supported a full-frame transfer speed of 30 frames per second using a 16-bit data range. However, higher imaging rates were possible by reading out user-defined smaller regions of interest (ROIs) from an image. The imaging sensors were thermoelectrically cooled down to and maintained at 0°C to suppress dark current. The cameras were fitted with identical 20.5 mm fixed-focal-length objective lenses (Schneider Optics, Van Nuys, CA) with an f/8 aperture. The cameras were positioned at a working distance of 650 mm from the surfaces of the scintillator tank (20 × 20 × 20 cm). The depth of field around the center of the tank was 205 mm. Figure 3.1 shows a schematic of the 3D scintillator detector, and the 3 unique image projections of the spot scanning proton beam.

The sCMOS cameras used in this study had an active pixel sensor architecture with each pixel having its own amplifier to convert charge into analog voltage. The sensor had a split readout scheme such that the top and bottom sensor halves were read out independently. Each column in each half of the sensor had column-level amplifiers and analog-to-digital converters. The sCMOS cameras were operated in a global shutter mode with working similar to that of an interline CCD sensor. At the start of the exposure all pixels in a frame began to accumulate charge and did so precisely for the duration of the exposure time. At the end of exposure, the pixels simultaneously transferred the charge to their readout nodes. Acquisition of each signal frame was preceded by a reference frame measurement. The reference frame measured the residual charge on the pixels after they were reset following the actual measurements. Since the same circuitry was used for reading out reference and signal frames, there was no place to hold the reference frame on the sensor and so a reference frame was first digitized and read out from the sensor and then the signal frame was digitized and read out from the sensor. The reference frame was subtracted from the signal frame to eliminate the influence of reset noise. This requirement for acquiring a reference frame for every signal frame limited the maximum achievable frame rate for the global shutter mode. To maximize the available frame rate the global shutter mode was configured to operate in an overlap mode. In the overlap mode, the exposure for the next frame

was carried out while exposure from the previous frame was being read out from the readout node. Since there was no on-board memory storage option on the cameras, the digital images were temporarily transferred and held on a computer RAM (128 GB capacity) using USB3.0 interfacing cables and were then spooled to the hard drive at the end of the imaging session.

A signal frame for our selected ROI (1100×1100 pixels) had a minimum exposure time of 5.082 ms and an additional 5.082 ms time to measure the reference frame. The ROI dimensions were selected to cover the entire tank area (20×20 cm). Since the sensor was set to work in an overlap mode, the minimum exposure time for the image frame was therefore restricted to (2×5.082 ms) along with an additional time for switching between the signal and reference frames ($83.2 \mu\text{s}$). The minimum exposure time was therefore 10.247 ms (2×5.082 ms + $83.2 \mu\text{s}$). A $2\text{-}\mu\text{s}$ charge transfer time was introduced between 2 consecutive signal frames. Thus, the dead time between frames was $85.2 \pm 10 \mu\text{s}$ ($2 \mu\text{s} + 83.2 \mu\text{s}$).

4.2.3. Camera Triggering

To trigger our cameras, we used a synchrotron-generated transistor-transistor logic (0-5 v) signals along with DM signals. We will call the synchrotron-generated signals the START and STOP signals to indicate the beginning and end, respectively, of the proton spot sequence for a given proton energy layer (or spill). We supplied the START signal and DM pulses to Arduino Uno microcontroller (300 kHz sampling rate) to control the camera acquisitions. The synchrotron generated the START signal approximately $500 \mu\text{s}$ before the actual spot deliveries. This time delay was more than sufficient to accommodate the internal camera delay ($2 \mu\text{s}$), which is the time duration the camera needs to respond to the trigger signals (here, START). The STOP signal was generated upon completion of all the spot deliveries in a spill. The trigger signals were monitored using an oscilloscope.

The DM pulses were used to keep a count of the number of spots delivered by the treatment plan. Depending on the dose required per spot, each spot may consist of a bunch of DM pulses. A

Schmitt trigger integrated circuit was used to eliminate the noise on these pulses before the microcontroller unit counted them. After receiving the START pulse, the microcontroller monitored the DM pulse deliveries every 1 ms to check the status of the spot delivery. The DM pulse readout by the microcontroller indicated active spot delivery, and absence of DM pulses indicated completion of the spot delivery. At the end of spot delivery, the microcontroller updated the measured spot counts and compared them to the total number of spots set by the user in the form of an array. If the spot counts reached the value specified in the array, the microcontroller sent a trigger signal to the camera, which effectively ended the current image exposure and started a new image. This new image corresponded to the next value in the array. Using this method, the number of spots delivered by the synchrotron could be reliably counted. Figure 4.2 is a flowchart illustrating the trigger scheme, and figure 4.3 is a timing diagram showing all the signals used for triggering.

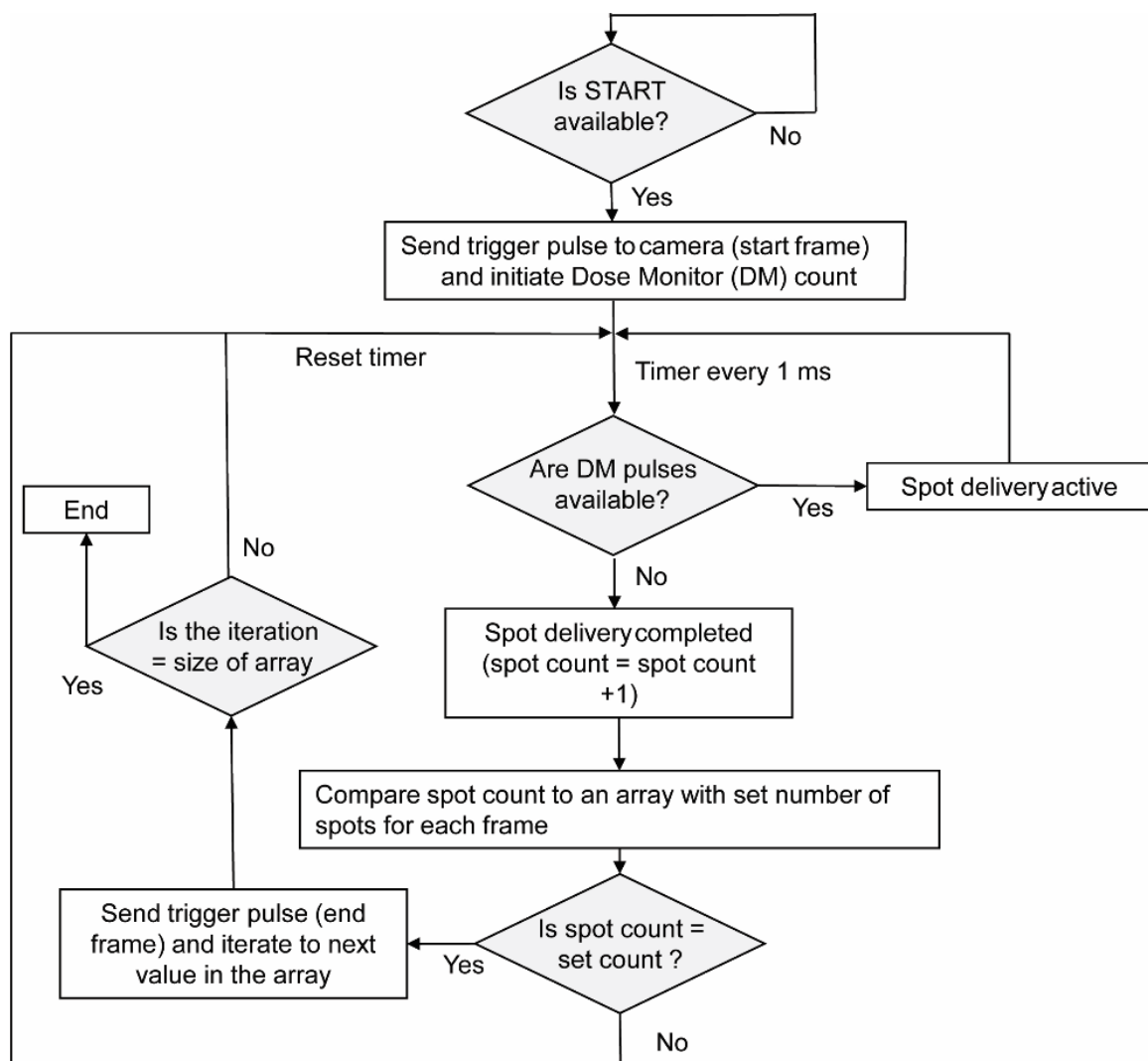


Figure 4.1 A flowchart describing the camera triggering and proton spot counting scheme developed in this study.

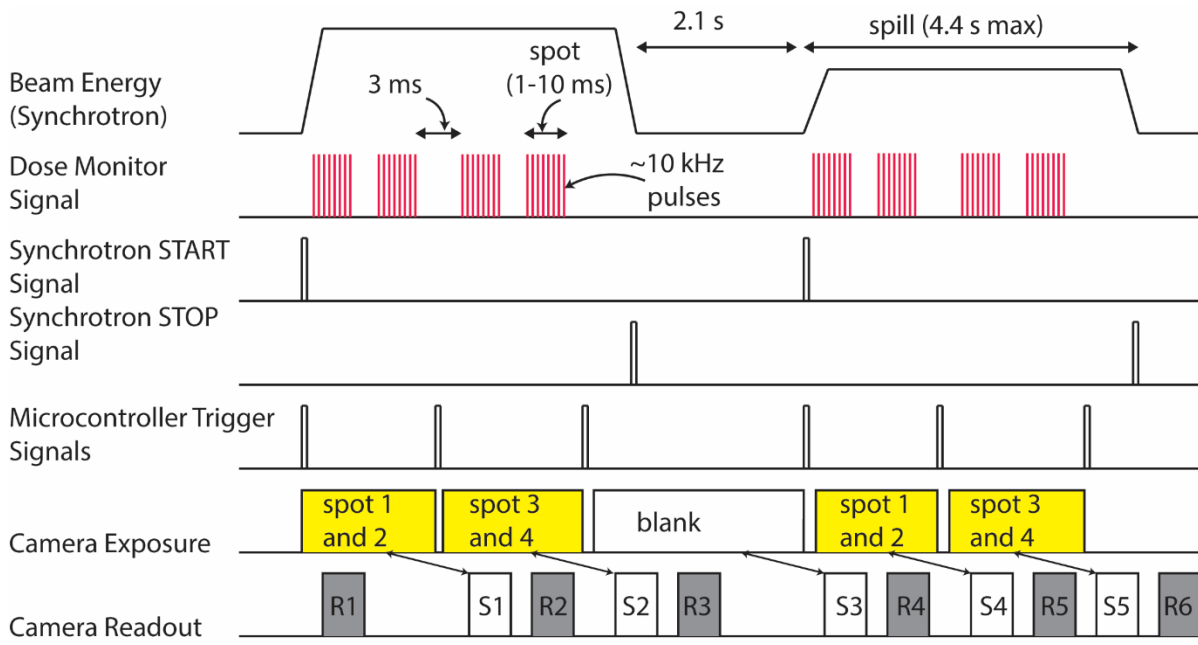


Figure 4.2 Timing diagram of the sCMOS trigger synchronization with synchrotron-generated signals (START and STOP) and dose monitor pulses. This example shows 2 energy layers with 4 spots each. The trigger is set to capture 2 spots in a frame. The camera readout shows the signal frames (S) and reference frames (R).

4.2.4. Beam delivery settings: trigger testing

To test this trigger scheme and demonstrate its usefulness, the detector was exposed to 5 proton beam energies (161.6, 140.9, 124.0, 100.9, and 85.6 MeV). Each energy was delivered with 2 MU (0.04 MU/spot), that consisted of 50 spots per energy. The mean signal intensity for each energy was compared using the triggering scheme and without the triggering scheme by setting the image acquisitions to the maximum frame rate (96 fps). The maximum frame rate setting captured the 50 spots in multiple frames and was expected to suffer signal loss due to the presence of dead time (~ 0.1 ms) between the frames due to desynchronized acquisitions. The calculated signal loss was around 1% for the non-triggering scheme, however, an additional signal loss based on the signal to noise ratio (SNR) of the image pixels was also expected. The SNR relationship was tested by exposing the camera to a uniform pulsed light source (100 ms) within an integrating sphere. Two acquisition modes that

mimicked the conditions for the proton beam experiments were tested. The first acquisition mode was set to acquire 1 frame with 100 ms acquisition time. This mode was equivalent to the synchronized acquisition scheme. The second acquisition mode was set to record 10 frames with the minimum acquisition time (10.247 ms). The light source intensity was varied to acquire 6 different SNR levels. The percentage difference in the mean signal intensities between the two acquisition modes as a function of SNR was plotted, where $SNR = 20 \log \left(\frac{\text{signal} - \text{background}}{\sigma_{\text{background}}} \right)$. The σ is the standard deviation of the background signal.

An experiment to determine the variability in image intensities for each energy and location was conducted. The detector was exposed to the same 5 proton beam energies, with each energy delivered over 9 different locations in a 3×3 grid. The distance between spots was 1 cm. The beam scanned through the 9 locations 5 times, delivering 0.08 MU per location (2 spots with 0.04 MU per spot). This beam sequence imaging was performed 3 times. The mean signal intensity and standard deviation per location were measured. The standard deviation measured the intensity changes for the combined 15 images per location, which would confirm that each image captured 2 spots per location. Background images were acquired for the specific frame exposure time in trigger mode and for non-trigger mode (10.247 ms). The mean background signal for exposure times ranging from 1 to 1000 ms was also measured to quantify the change in the background intensity as a function of the exposure time. The aim was to simplify the background subtraction for trigger mode by using a single exposure time for all the images.

Proton beam images recorded in this experiment were processed by subtracting the background signal and then applying a median filter (3 by 3 pixels) to eliminate the influence of stray radiation on the sensor. The measurements were performed by turning off the lights in the treatment room. No other optical corrections, such as refraction, perspective, and lens distortion were applied

because only the relative mean signal intensities were compared (Robertson *et al* 2014). All image analyses were performed using MATLAB (version R2017b; MathWorks, Natick, MA).

4.3. Results

Table 4.1 shows the percentage difference (for each camera) between the mean intensity of the signal using the trigger and non-trigger modes. The mean intensity measured using the trigger was $10\% \pm 0.4\%$ higher than without the trigger in camera X and $11.9\% \pm 0.8\%$ for Camera Y. The relative difference in mean intensity for camera Z was seen to vary with the beam energy. Camera Z integrates the light along the beam path, which will result in higher signal intensity for high energy beams than low energy beams (see figure 4.4). Figure 4.4 plots the integrated depth dose profile and lateral profile of the 5 energies processed projections. Thus, better image SNR was obtained with the higher beam energies. Figure 4.5 demonstrates the percentage signal difference as a function of SNR in a single 10.247 ms frame between triggered acquisition (1 frame at 100 ms) and non-triggered acquisition (10 frames at 10.247 ms) for a 100 ms duration uniform light source. The results of figure 4.5 are due to the increased variance in the pixel intensity as the light intensity approaches the noise floor.

Figure 4.6 illustrates the normalized mean intensity and standard deviation for all 5 energies as a function of spot location for camera X. The mean signal intensity was normalized to the central spot for each depth of the grid pattern to account for intensity changes resulting from uncorrected light intensity attenuation. As expected the lowest beam energy produced largest errors because of the least SNR available for these images. The recorded signal intensity was uniform as a function of the beam location with less than 2% variation per location. This suggested that the trigger is capable of capturing the specified number of spots per image and per location. The other 2 cameras showed similar response.

A mean background signal of 122.5 ± 3.2 pixel intensity for a 1-ms exposure time was measured. With increasing exposure times, we measured a small increase in the mean background

signal, as shown in Table 2. The average maximum pixel value for all exposure times was 150 ± 2 pixel intensity. These results indicated that the background signal is independent of the camera exposure time and could therefore be used as a fixed exposure time for background subtraction in the future.

Table 4.1 The mean percentage difference in the mean intensity measured using trigger mode and non-trigger mode for 5 proton beam energies with 50 spots per energy. The measurements were performed 3 times.

Energy (MeV)	% difference in mean intensity between trigger and non-trigger modes		
	Camera X	Camera Y	Camera Z
161.6	9.5 ± 0.3	11.3 ± 0.3	2.8 ± 0.1
140.9	9.6 ± 0.4	11.2 ± 0.1	4.3 ± 0.3
124.0	10.1 ± 0.3	11.6 ± 0.3	5.4 ± 0.2
100.9	10.5 ± 0.1	12.9 ± 0.3	10.1 ± 0.3
85.6	10.2 ± 0.2	12.6 ± 0.3	12.1 ± 0.2

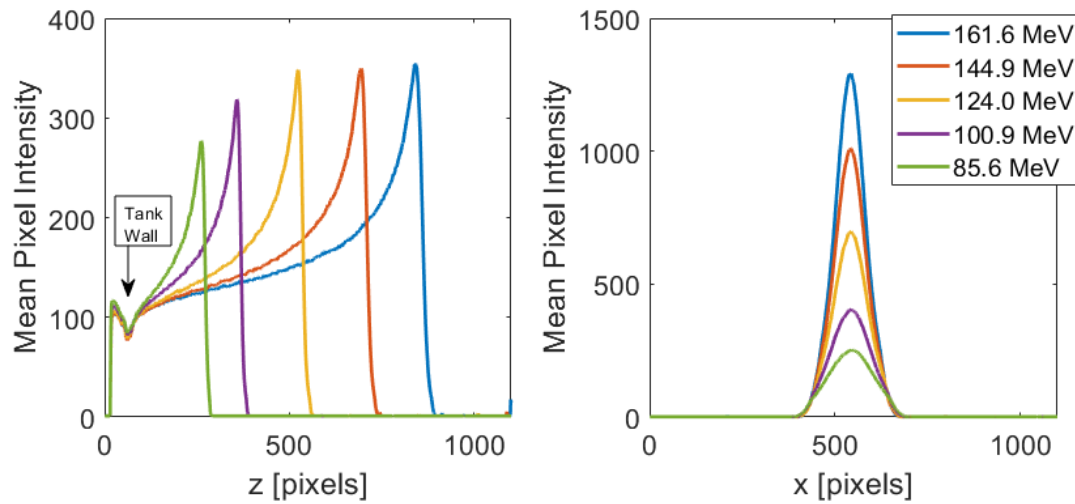


Figure 4.3 The processed integrated depth dose curves (projection X or Y) and lateral profiles (projection Z) as captured by the scintillator detector.

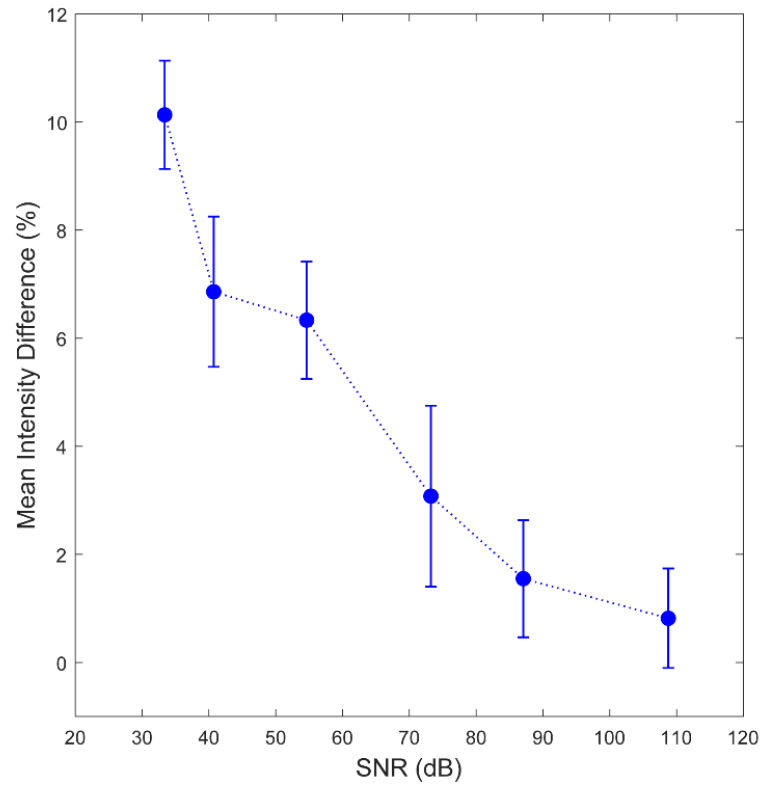


Figure 4.4 The percentage difference between trigger and non-trigger modes as a function of the SNR for the 10.247 ms frame. The errorbars represent the standard deviation over 5 measurements.

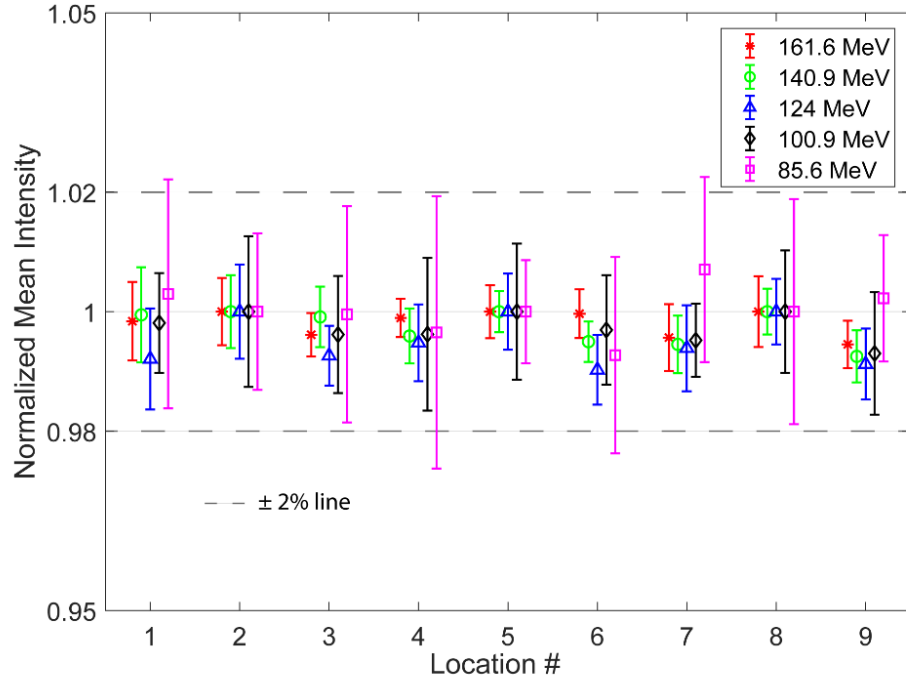


Figure 4.5 Normalized mean intensity of 2 spots (0.08 MU) in an image which was repeated 4 times in a run per location. The experiment was performed 3 times resulting in a total of 15 images per location for each of the 5 beam energies. The results shown are for camera X. The signal was normalized to the middle spot of the 3 spot locations along the x-axis. The other 2 cameras showed similar response.

Table 4.2. Background signal measurements for different exposure times. The percentage increase was calculated relative to the 1-ms exposure time measurement.

Exposure time (ms)	Mean pixel value	Standard deviation	Max pixel value	Percentage increase of mean pixel value
1	122.5	3.2	151.0	-
5	122.6	3.0	148.5	0.1%
10	122.6	3.0	148.0	0.1%
400	123.1	3.2	150.5	0.5%
800	123.2	3.3	152.5	0.5%
1000	123.2	3.4	152.5	0.6%

4.4. Discussion

In this work, we implemented a spot counting solution for camera triggering that allowed us to: (1) automate dynamic imaging of all the proton spots delivered in a treatment plan, (2) combine multiple proton beam spots into a single camera frame, and (3) generate significantly fewer frames. The advantage of this approach is that it uses DM pulses to count and track delivery of each spot, which is clinically used for beam delivery. This synchronization dynamically alters the camera exposure times to perfectly match the delivery times for spots delivered to any location. This increases the image SNR by restricting the imaging times to beam delivery intervals.

To maximize the acquisition speed, the camera was operated in an overlap imaging mode that used global shuttering and an external trigger. With these settings, the minimum exposure time for a frame was 10.247 ms for the selected ROI. For a typical spot delivery time of 4 ms and with the aforementioned camera limitations, it was not possible to decouple and capture a single proton spot in a frame from a bunch of successive spot deliveries. However, a minimum of 2 consecutive spots could

be combined into a frame. If the spot was delivered in less than 4 ms, e.g. 1 ms delivery time, then 3 spots (after accounting for a 3-ms interval after every spot) could be captured in a single camera frame.

The dead time between frames was around 0.1 ms, which suggested that the amount of light missed would only be 1%. However, our study showed that image SNR also has an impact on the signal loss (Moomaw 2013). A characteristic of the sCMOS used in this study is the dual amplifier readout. Briefly, a sCMOS camera digitizes signal simultaneously through two overlapped 11 bit analog to digital converters (ADC), one is specifically 'low noise', and the other is 'high well capacity'. This provides the camera with a wide dynamic range. The region where the 'low noise' amplifier takes over will have the larger variance buffered by the statistic outliers being read through the low noise ADC. This is demonstrated in figure 4.7, which is the results of the intensity difference per pixel between trigger and non-triggered acquisition of the 161.6 MeV proton beam using camera Z. As the light levels decrease the variance increases; additionally, the distribution becomes less Gaussian and more Poisson. This study demonstrated that a triggered single long exposure of multiple spots essentially increased SNR compared to non-triggered mode set to acquire the same number of spots. Thus, the mean signal intensity for the trigger mode is higher than the non-trigger mode. For a spot with 0.04 MU setting typically used in the treatment plan, the signal intensity has a relatively low SNR (~20 dB), and the measured intensity loss would be around 10% (refer figure 4.5) for an un-synchronized image acquisition. Therefore, trigger synchronization is important for accurate dosimetry.

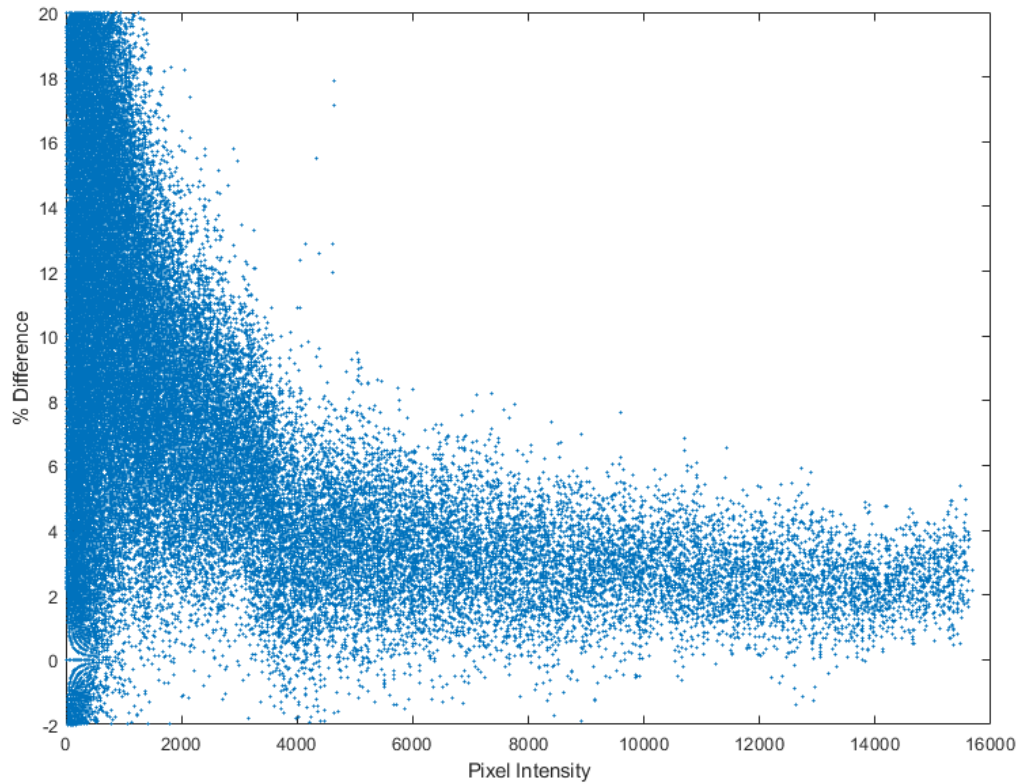


Figure 4.6 Intensity difference between triggered and non-triggered acquisition for Camera Z exposed to 161.6 MeV beam as a function of pixel intensity. The overlap region of the two ADCs is around 4000 a.u.

4.5. Conclusion

We demonstrated a flexible triggering scheme for a camera and scintillator detector system for use with scanning proton beams which ensured that all the beam deliveries were captured for accurate dosimetry. This system, which used an open hardware microcontroller therefore allows for efficient and simple quality assurance and treatment plan verification measurements.

Chapter 5 : Ionization Quenching Correction factors

5.1. Introduction

Dosimetry detectors utilizing volumetric scintillators are of growing interest because they can offer fast, high-resolution and accurate measurements of absorbed dose distribution through optical imaging (Beddar *et al* 2009, Pönisch *et al* 2009, Archambault *et al* 2012, Hui *et al* 2015, Darne *et al* 2017, Fukushima *et al* 2006, Almurayshid *et al* 2017). However, the light emitted in the scintillator medium exposed to proton beams, or any heavy charged particle, exhibit a nonlinear response with the incident radiation ionization density (Birks 1964). For proton and heavy charged particles, the ionization density is quantified as the linear energy transfer (LET), which varies as a function of depth. The LET increases rapidly at the Bragg peak (BP) region, resulting in an under response of light emission by the organic scintillator. This phenomenon is called ionization quenching and it must be addressed to utilize 3D volumetric scintillator detectors for dose verification.

Robertson *et al* demonstrated that quenching correction was possible using Birks equation (Birks 1964) in a volumetric liquid scintillator, and found dose agreement within $\pm 3\%$ at the Bragg peak for high energy beams and $\pm 10\%$ for the 85.6 MeV beam (Robertson *et al* 2013). Similarly, Wang *et al* showed errors between the corrected light signal (using Birks equation) and the calculated dose to within $\pm 5\%$ in a polystyrene based scintillating fibre exposed to single energy passive scattering proton beams (Wang *et al* 2012, Robertson *et al* 2013). Almurayshid *et al* also demonstrated quenching corrections using Birks equation with a volumetric plastic scintillator and commercially available camera for a 60 MeV proton beam (Almurayshid *et al* 2017). They reported a 0.2 mm range accuracy and 3% Bragg peak/plateau ratio accuracy.

The non-linear response of organic scintillators has been explained well by the widely used semi-empirical model proposed by Birks. The models relate the non-linear response to the average energy loss per unit length (dE/dx). The model was extended by Chou to relate quenching effects to a second order of (dE/dx) (Chou 1952). Later, Blanc *et al.* proposed a more general model of scintillation

by looking at the kinetics of ionization quenching (Blanc *et al* 1964). The model accounted for the temporal aspect, and radial diffusion of energy deposition. The simplified version of Blanc's formula becomes the Birks' equation. Christensen and Andersen demonstrated the use of Blanc's model and its advantages for fibre-coupled scintillators exposed to proton beams (Christensen and Andersen 2018). The evidence of the non-linear response of scintillator depending on not just (dE/dx) , but the particle type led to exploring other properties of the energy loss process for different particles with the same dE/dx . This property is the energy deposition by secondary electrons. Michaelian and Menchaca-Rocha formalized an analytical model of ion-induced luminescence, which was termed the energy deposition by secondary electrons (EDSE) (Michaelian and Menchaca-Rocha 1994, Michaelian *et al* 1995). Regions close to the particle track (high energy deposition density) are the source of the non-linearity of scintillation.

In this study, we have developed a large volume organic liquid scintillator detector (LS) that has the capability to image 3D dose distributions of proton beams in real time (Darne *et al* 2016). The prototype 3D scintillator detector is based on previously studied and characterized volumetric scintillator detector for verification of proton beam properties (Beddar *et al* 2009, Pönisch *et al* 2009, Archambault *et al* 2012, Robertson *et al* 2014). In this work we will be exploring two different ionization quenching models (Birks equation and EDSE model) for use in volumetric scintillator detectors. We will also investigate the effects of optics to specify the values of dose and LET in each pixel.

5.2. Methods

5.2.1 3D Scintillator Detector

A detailed description of the detector and characterization has been described earlier in chapter 3. The 3D scintillator system is made of an acrylic tank (20 cm × 20 cm × 20 cm) that has three clear sides and three opaque black acrylic sides. The tank was filled with Optiphase Hisafe 3 liquid scintillator (PerkinElmer, Waltham, MA). To image the light distribution, three Zyla 5.5 scientific complementary

metal oxide semiconductor (sCMOS) cameras were used (Andor Technology Ltd., Belfast, UK). For this study, we are only interested in projection x (z-y plane), which shows the depth dose distribution, for ionization quenching corrections. The cameras were equipped with a 20.5 mm fixed-focal-length objective lens (Schneider Optics, Van Nuys, CA) and an f/8 aperture. The cameras were positioned at 65 cm away from the tank surface. This resulted in a depth of field of 20.5 cm around the center of the tank. The mean spatial resolution of the system was 0.208 mm.

5.2.2 Irradiation conditions and Monte Carlo Simulations

The scintillator detector was exposed to the spot scanning proton beam at UT MD Anderson Cancer Center- Proton therapy center. The proton beam system can generate 94 proton beam energies ranging from 72.5 MeV to 221.8 MeV. For this study, proton pencil beams were measure and modeled based on the scanning beam nozzle at the Proton therapy center. The energies chosen were 85.6, 100.9, 144.9, and 161.6 MeV. These energies were chosen because they will span across the size of the scintillator tank (20 cm) and are a reasonable sub-sample of the range of energies possible.

Proton beam dose distribution and track averaged LET in 3D were determined using a validated Monte Carlo radiation transport code MCNPX, version 2.7d (Sawakuchi *et al* 2010). The geometry setup of the scintillator detector was reproduced in the MC code. The face of the detector was placed at the isocenter at source-to-surface distance of 270 cm. The voxel size was $1 \times 1 \text{ mm}^2$ laterally to the beam, and in the axial direction the resolution was 1mm in the build-up region and 0.1 mm in the Bragg peak. The number of protons simulated was 5×10^7 for each beam energy, resulting in an uncertainty of less than 1% for all voxels with doses exceeding 2% of the maximum dose.

5.2.3 Image processing: Optical simulation

A previously established optical artefact corrections and geometric calibration technique were used to correct acquired images (Robertson *et al* 2014, Hui *et al* 2015). The optical corrections included corrections for refraction at the air-scintillator interface, and image perspective. The lens distortion was

corrected using the Camera calibration Toolbox for MATLAB (Bouguet 2010). The geometric calibration determined the optical length from the surface of the tank to the camera sensor, angular shift, and translational shift of the tank relative to the camera sensor center.

The parallax errors in projections will hinder the alignment of MC dose and LET with camera projections. This is demonstrated in figure 5.1, where the integrated depth dose profiles are orthogonal to the measurement plane. However, for the scintillator system, the shape and volume of the integrated plane are not orthogonal to the beam axis and are different depending on the location of the measurement. This artefact cannot be corrected for because the projections are already an integrated signal of the light distribution. If the Bragg peak was at the center of the system then it is expected that this artefact will be less. To test this, the 4 proton beam energies were acquired such that the center of the Bragg peak falls on the center of the camera sensor. This will not completely eliminate the artefact. Therefore, in addition to comparing central and non-central Bragg peak projections, the simulated 3D dose and average LET distribution was used to obtain a simulated projection that matches the scintillator system using the aforementioned optical-chain calibration. A central plane from the 3D distribution was projected onto a single row of camera pixels to obtain the average LET, and dose profile using a projection matrix that contained refraction, and perspective optical artifacts only (i.e. only geometric information were used to determine the average LET and Dose in the non-orthogonal volume for the scintillator system).

The scintillation light will be plotted as a function of LET for each case to demonstrate the parallax error effect on the assignment of LET values. All Image processing and analyses were performed using MATLAB (version R2017b; MathWorks, Natick, MA).

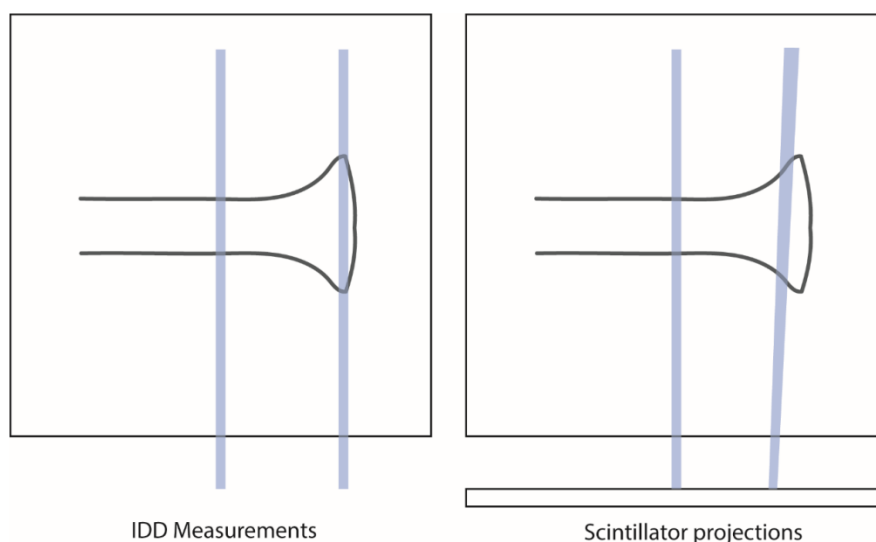


Figure 5.1 A schematic of integrated depth dose (IDD) measurements compared to the scintillator projections. The IDD measurements present an orthogonal projection of the dose, while the scintillator detector projections are displaced due to the use of an objective lens. The scintillator projections are a result of integrating along a different volume depending on the location of the beam.

5.2.4 Quenching Correction

In this study, two scintillation models, described in the sections below, will be used to determine the quenching correction factors. The first model is the semi-empirical model developed by Birks (Birks 1964). This model is very successful in correcting quenching for a given ion. The second model is more recently developed by Michaelian and Menchaca-Rocha, which is called the EDSE model (Michaelian and Menchaca-Rocha 1994). The main advantage of the EDSE model over Birks' model is that it can be used to correct the response of scintillators exposed to a variety of heavy charged particles with one free parameter. In contrast, the Birks' model quenching parameter will have to be fitted with an arbitrary function to obtain the quenching parameter for each ion (Michaelian and Menchaca-Rocha 1994, Boivin *et al* 2016). Therefore, the EDSE model could result in greater accuracy. The model quenching parameters will be determined by fitting the light produced in a voxel as a function of LET. The models

will be compared quantitatively by comparing the depth-dose profiles, and the 95% confidence interval of the quenching parameters fit.

5.2.4.1 Birks equation

The Birks model (described in chapter 2) is given by the following equation,

$$\frac{dS}{dx} = \frac{A \frac{dE}{dx}}{1 + kB \frac{dE}{dx}} \quad (5.1)$$

where $\frac{dS}{dx}$ is the scintillation yield per unit length, A is the light production efficiency, and kB is the quenching factor. The quenching factor is unique to the type of scintillator used, and the type of incident particle. The Birks equation can be rewritten in terms of finite volume as follows,

$$S_v = \frac{A LET_v}{1 + kB LET_v} \phi_v \quad (5.2)$$

where S_v is the light emitted in a volume v , LET_v is the track average LET in that volume, and ϕ_v is the particle fluence in that volume.

5.2.4.2 EDSE equation

The EDSE model relates the ionization quenching to the deposition of energy by the secondary electrons along the track of the ion beam. The EDSE model assumes that the regional density of excited molecular structures (energy carrier density) is proportional to the local energy deposition density in the absence of quenching effects. The derivation of the electron energy density as a function of radial distance is based on an incident ion colliding with electrons in medium delivering an impulse. The residual energy of the electron along the radial track is based on Lindhard's potential theory, and Kanaya and Okayama semi-empirical parametrization (Kanaya and Okayama 1972). The EDSE model also includes terms for electrons backscatter. The resulting electron energy density as a function of radial distance is given as,

$$\rho(r) = D \frac{1}{r^2} \left[1 - \frac{r}{R_{\max}} \right]^{d+\frac{1}{n}} \quad (5.3)$$

The value D is,

$$D = \mathcal{N} \frac{e^4}{nm_e} \frac{z^{*2}}{V^2} \quad (5.4)$$

where m_e is the electron mass, \mathcal{N} is the number of electrons per unit volume, z^{*2} is the effective charge of the ion, and V is the ion velocity. R_{\max} is the maximum range of the secondary electron, and $d=0.045 Z_{\text{eff}}$, where Z_{eff} is the effective atomic number of the medium. This equation is valid from the minimum impact parameter b_{\min} to R_{\max} . The minimum impact parameter is the minimum distance of approach of the two particles. Integration over the radial distribution is equal to the specific energy loss, or LET for protons.

Then the energy carrier density per unit path length of the ion is given as,

$$\frac{dN_e}{dx} = D \left[\pi r_q^2 \rho_q + \int_{r_q}^{R_{\max}} \rho(r) 2\pi r dr \right] \quad (5.5)$$

where ρ_q is the quenching parameter that is specific to the scintillator detector, and r_q is the corresponding distance at which the energy deposition density falls below the quenching density. This equation is a result of the integral of $\rho(r)$ in two parts: the first part is the quenched region ($0 \leq r < r_q$), and the second part is the unquenched region ($r_q \leq r \leq R_{\max}$). Finally, the scintillation yield per unit length is $\frac{dS}{dx} = A \frac{dN_e}{dx}$. The value A is the scintillation efficiency. The integral in equation 5.5 can be solved analytically if the power in equation 5.3 is a rational number. For plastic scintillators this value can be approximated to $\frac{3}{4}$ ($Z_{\text{eff}} = 3.5$ giving $d + \frac{1}{n} = 0.7575$). Michaelian and Menchaca-Rocha have carried out this integral analytically for common organic and inorganic scintillators (Michaelian *et al* 1995).

Similarly to Birks equation, we can rewrite this model in terms of a finite volume as follows,

$$S_v = A N_{ev} \phi_v \quad (5.6)$$

where N_{ev} is the average value of energy carrier density in that volume.

5.2.5 Quenching Correction factor

To determine the quenching correction factors per voxel, the quenching parameters for each model (k_B for Birks' model, and ρ_q for EDSE model) will be determined using non-linear least square fitting of the measured scintillation light profile compared to the simulated scintillation light profile. The energy deposition in a voxel can be obtained by multiplying the track averaged LET and particle fluence through that voxel as follows,

$$E_v = LET_v \cdot \phi_v \quad (5.7)$$

Therefore, the quenching correction factor using the Birks equation will be,

$$QCF_v = \frac{1 + k_B LET_v}{A} \quad (5.8)$$

Similarly, the EDSE model quenching correction factor per voxel can be determined by combining equation 5.6 and 5.7,

$$QCF_v = \frac{LET_v}{A N_{ev}} \quad (5.9)$$

5.3. Results

5.3.1 Optical Corrections

Figure 5.2 demonstrates a depth dose distribution and the light distribution, along with the LET for a 100.9 MeV proton beam. This projection will be called the original projection, which includes the optical corrections applied to it. The results of the Bragg peak central projections compared to the original projection are shown in figure 5.3. Due to parallax error the Bragg peak scintillation signal was higher for the BP central projections and varied as a function of beam energy (1-8%). Furthermore, the original projection's Bragg peak width was wider by 2.87 ± 1.7 mm.

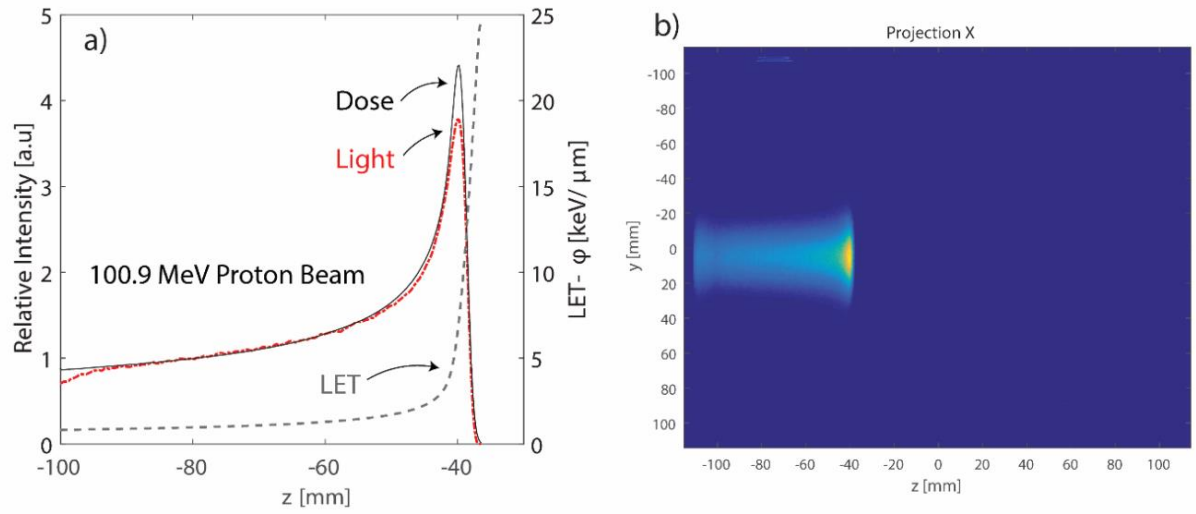


Figure 5.2 a) The depth dose profile of a 100.9 MeV proton beam, along with the scintillation light and LET curves. **b)** The corresponding projection from the 3D scintillator detector (z-y plane, projection x).

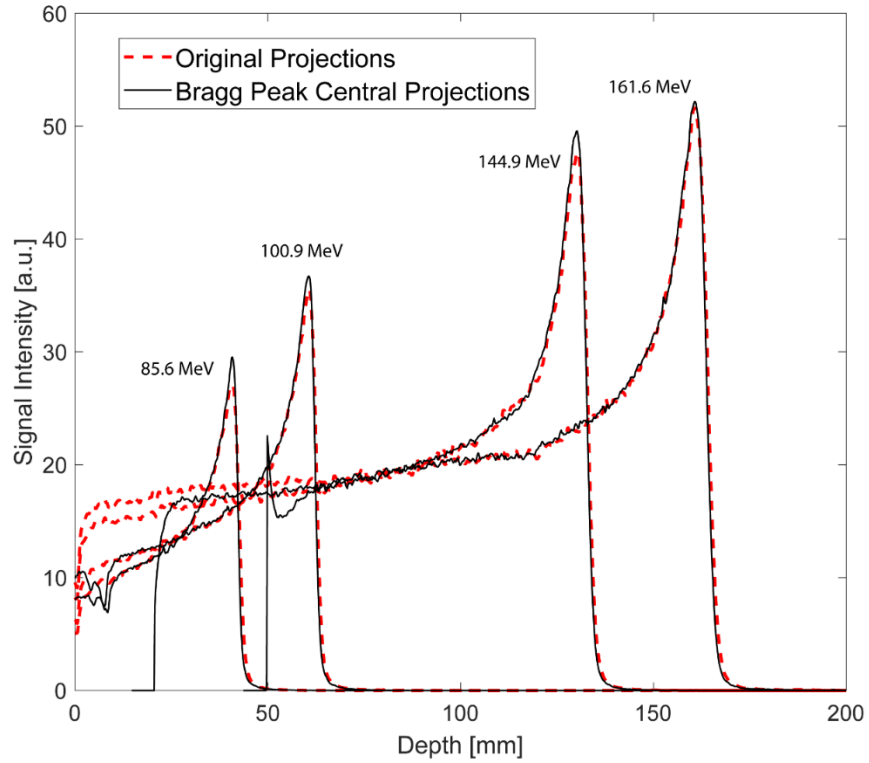


Figure 5.3 the central axis depth dose curves of the measured scintillation signal for the original projections of the 3D scintillator detector and shifted projections that align the Bragg peak at the center of the camera. The Bragg peak central projections are sharper than the original projections.

5.3.2 Quenching Model fitting

The quenching parameters for each model were determined by fitting the scintillation light of each beam energy. The points included in the fitting were only up to the distal 80% of the Bragg peak. The reason for this cutoff was to minimize the uncertainty due to low level of scintillation light. The major error was found around the Bragg peak and distal edge. Figure 5.4 shows the effect of optics on the assignment of LET values for each voxel. The Bragg peak central projections (shown as unfilled markers) did not diverge as much as the original projections due to the parallax error.

The best fit was obtained by comparing the scintillation light to a simulated projection (i.e. averaging the LET and dose along the non-orthogonal projections) as shown in figure 5.4 (b). Therefore, confirming that the average LET value in a volume can be used to explain the scintillation response.

The measured kB parameter was $0.083 \pm 0.003 \mu\text{m keV}^{-1}$ (95% confidence interval) with a normalization factor $A = 209$. The quenching parameter for the EDSE model was $23.4 \pm 5.7 \text{ keV } \mu\text{m}^{-3}$ (95% confidence interval) with a normalization factor of $A = 341$. The higher error in the EDSE model parameter fit is due to some model simplifications to determine the electron radial distribution. Furthermore, the ion energy was assumed to be mono-energetic for each voxel.

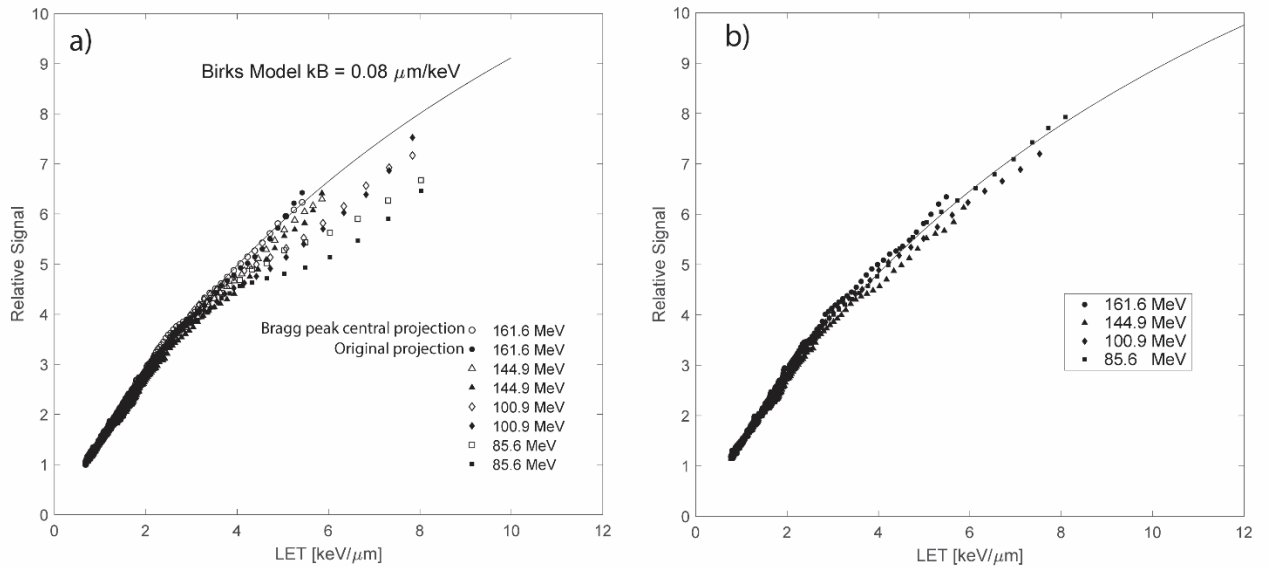


Figure 5.4 The measured scintillation light signal as a function of LET for proton beam energies along with the curve fitting using Birks semi-empirical model. **a)** plots the measured scintillation signal of the original projections (filled markers) and the Bragg peak central projections. **b)** shows the scintillation signal of the original projections as a function of LET that have been averaged along the central axis according to the parallax displacement.

5.3.3 Quenching correction factors

Figure 5.5 plots the depth dose curves at the central axis for the 4 beam energies tested in this study.

The quenching correction factors were applied to correct the scintillation signal. Both quenching models were plotted. The ratio of the dose as determined by Monte Carlo over the corrected dose using both models was also plotted in figure 6. The Bragg peak percent dose difference was within $\pm 3\%$ for Birks model and $\pm 6\%$ for EDSE model. Table 5.1 is the Bragg peak percent dose difference from Monte Carlo for uncorrected and corrected scintillation signal per proton beam energy.

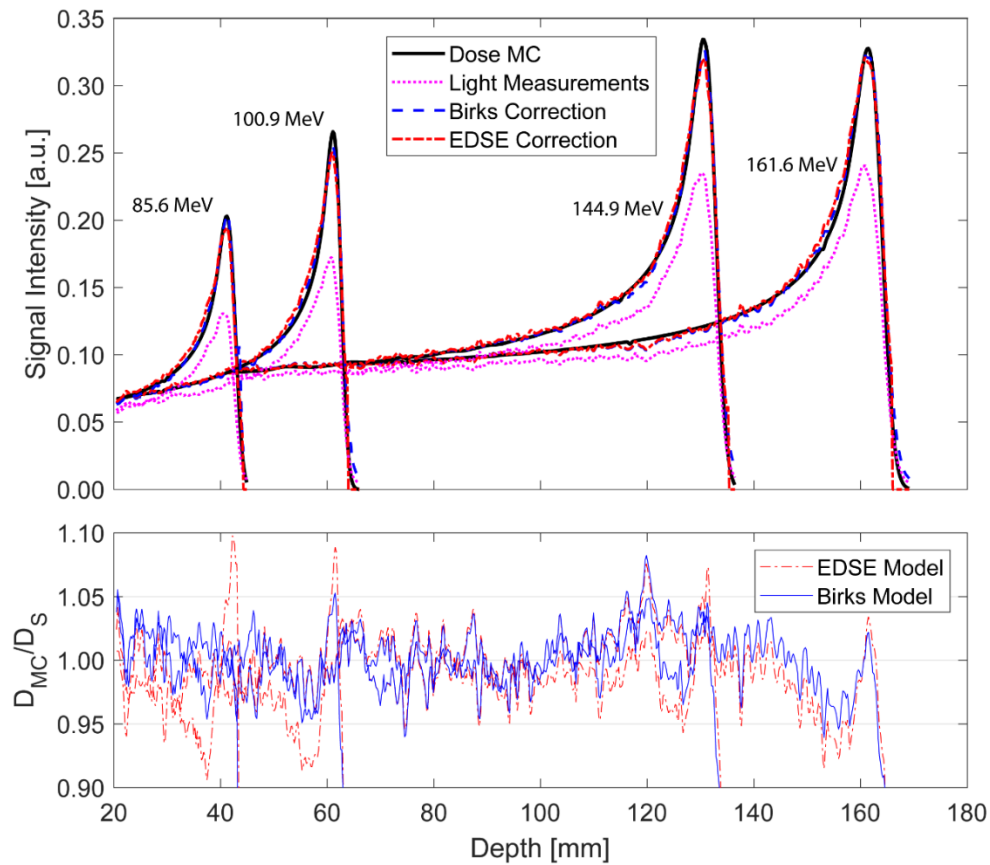


Figure 5.5 (Top) The depth-dose profiles at the central axis for each proton beam energy. The dose calculated using MC simulation is compared to the corrected and uncorrected scintillation signal using

the Birks model and EDSE model. **(Bottom)** The ratio of the MC dose (D_{MC}) to corrected dose of the scintillator (D_s) for both models tested in this study.

Table 5.1 The percent difference from Monte Carlo of the Bragg peak height for each beam energy using the Birks and EDSE quenching correction factors

Energy [MeV]	Bragg peak percent difference from Monte Carlo		
	Uncorrected	Birks Corrected	EDSE Corrected
161.6	40.44	0.17	0.86
144.9	42.57	3.00	4.87
100.9	56.75	2.60	5.25
85.6	57.92	0.43	3.85

5.4. Discussion

The major source of error in this study is the assignment of LET values for each voxel in the projection. The simulated projection showed that an average LET value can still be utilized to correct for quenching (as demonstrated in figure 5). Unfortunately, acquired projections cannot be corrected for parallax errors due to the projection having already integrated the light distribution. The fact that volumetric scintillator detectors are fast detectors (i.e. Measuring all 94 beam energies can be done in a few minutes), make it feasible to use the 94 proton beam energies to generate a calibration ‘look up table’ of quenching correction factors based on the ratio of the scintillation response to dose. This will require further testing the stability and reproducibility of light measured and the calibration factors. For proton range verification the detector has been shown to be reproducible and with sub-millimeter accuracy for all 94 beam energies (Darne *et al* 2017, Hui *et al* 2015).

Birks’ equation prevails over the EDSE model in this study in terms of accurately reproducing the depth dose curve. Some factors that limited the accuracy of the EDSE models are the oversimplification and approximations of the general expression of the electron energy deposition density per unit path length of the incident ion as a function of radial distance. The energy straggling

and range straggling were not included in this model. In this study the Monte Carlo LET values were used to alleviate this problem by normalizing the quenching correction factors based on the EDSE model multiplied by LET as shown in equation 5.9. Although it proved less accurate than Birks' model in this study, the EDSE model or similar models that are based on track structure could provide a better understanding of ionization quenching for high LET values ($> 12 \text{ keV}/\mu\text{m}$), for example in Carbon ion beams.

The proton beam used in this study and a previous study by Robertson *et al* (Robertson *et al* 2013) is from a synchrotron based proton beam accelerator, while Almurayshid *et al*'s proton beam was produced using a fixed proton beam cyclotron (Almurayshid *et al* 2017). For fixed beam cyclotron accelerators, the shape (axial and lateral width of the beam) of the proton beam will not change as a function of beam energy. An energy degrader is used to change the energy (or range) of the beam. In contrast the synchrotron will accelerate protons to each specified energy, leading to a different energy spectrum. A wide energy spectrum will result in a broader Bragg peak. Therefore, the shape of the beam will be energy dependent.

Optical parallax error was affecting the lower beam energies more so than the high beam energy. For low beam energies, this effect is exacerbated because the Bragg peak width for low beam energies is sharper than for higher energies. In the future, the 3D reconstructed light distribution using Maximum Likelihood Expectation Maximization (MLEM) should improve the assignment of LET per voxel, which will improve quenching measurement accuracy in volumetric scintillators (Hui *et al* 2014).

5.5. Conclusion

In this study, the ability to correct for quenching was demonstrated for volumetric scintillator detectors using Birks' equation and the EDSE model. The Birks's equation with the use of an average LET value in a voxel provided better accuracy than the EDSE model at reproducing the depth dose curves. The camera parallax errors are the major source of uncertainty for low proton beam energies with sharp

Bragg peak, and steep LET curve. The non-orthogonal projections captured using objective lens makes quenching correction complicated for projection images. The study demonstrated that simulated average LET, and dose projections compared to the measured projections showed that the response of the scintillator depends on the average LET values in that volume.

Chapter 6 : Conclusions and future directions

6.1. Summary and Conclusions

In this work, we developed a 3D liquid scintillator-based detector for fast synchronized acquisition of discrete spot scanning proton beam systems. Significant steps were taken to translate this detector for clinical applications in proton therapy, in particular, patient specific dose verification. Ionization quenching is one of the major limitations for ion beam dose verification accuracy using scintillators. This study used established ionization quenching models and implemented them for volumetric scintillators. However, in order to relate the scintillation light output to dose, the system setup was characterized and improvements in acquisition setup were developed.

The characterization study established the system capabilities of high spatial (0.21 mm) and temporal resolution (10.25 ms). The large scintillator volume covers most treatment plans. The system was portable and durable and provided real-time measurements. The study identified and analyzed several performance criteria such as spatial and temporal resolution, stability (1%), SNR (20 dB at 0.5 cGy), and dose response linearity (99.6%). The proton beam range verification was with an average error of -0.07 ± 0.03 mm. All 94 proton beam energies can be measured in a few minutes with this system. The inclusion of the third camera facilitated the measurement of the 3D location of the beam position within the detector with good accuracy.

The second study demonstrated the ability to synchronize camera acquisition with beam delivery. A flexible triggering method was developed for a camera and scintillator detector system to ensure that all the beam deliveries were captured for accurate dosimetry. This system, which used an open hardware microcontroller, allows for efficient and simple quality assurance and treatment plan verification measurements. Camera acquisition synchronization with beam delivery is important for accurate dosimetry. For example, the signal intensity has a relatively low SNR (~ 20 dB) for a typical spot

with 0.04 MU, which will have a measured intensity loss of $\sim 10\%$ for an un-synchronized image acquisition. Overall, the synchronization demonstrated accurate measurements of the light intensity.

The final study corrected the scintillation light emission using the widely known ionization quenching model by Birks. The study also applied the EDSE quenching model. The Birks's equation with the use of an average LET value in a voxel provided better accuracy than the EDSE model at reproducing the depth dose curves. The camera parallax errors are the major source of uncertainty for low proton beam energies with sharp Bragg peak, and steep LET curve. The non-orthogonal projections captured using objective lens makes quenching correction complicated for projection images. The study demonstrated that simulated average LET, and dose projections compared to the measured projections showed that the response of the scintillator depends on the average LET values in that volume.

6.2. Future Directions

This project established the performance of the 3D scintillator detector, and improved acquisition setup. The addition of a third camera captures 3D information of the proton beam. The steps taken in this project are crucial to the development of a 3D reconstruction of the scintillation light output distribution using the measured projection data. A method was already developed by Hui et al to reconstruct the 3D light distribution using simulated data in ideal conditions (Hui *et al* 2014). However, further development is needed to account for the complexities of a real-world system, including internal reflections in the scintillator and camera tilt and offset. The reconstruction method applies a maximum a-posteriori (MAP) iterative reconstruction technique, which allows the reconstruction of a 3D light distribution based on a limited number of projection angles (Rudin et. al 1992, Bruyant 2002, Pierro and Yamagishi 2001, Hebert and Leahy 1989). The MAP algorithm uses projection matrices to relate the 3D light distribution inside the scintillator to the 2D image acquired by each of the cameras. The projection matrices will need to account for camera-related imaging artifacts including refraction, vignetting, lens aberrations, and blurring due to the lens point spread function (Robertson *et al* 2014).

Further modifications to include internal reflection, and geometric calibration (Hui *et al* 2015) are necessary to use the reconstruction method on measured data from this project.

The reconstructed light distribution will be the ideal data to relate the light intensity to energy deposition for each voxel. This will improve ionization quenching correction models for converting the measured light distribution into corresponding dose values. Specifying LET for voxels beyond the Bragg peak might still have higher uncertainty. Therefore, further understanding of ionization quenching in organic scintillators is warranted. Scintillation models can be explored to theoretically predict the light emission based on the kinetics of ionization quenching. These models will incorporate ionization quenching time dependence as rate equations to relate the radial diffusion of the deposited energy to scintillation (Blanc *et al* 1964, Christensen and Andersen 2018).

Bibliography

- Almurayshid M, Helo Y, Kacperek A, Griffiths J, Hebden J and Gibson A 2017 Quality assurance in proton beam therapy using a plastic scintillator and a commercially available digital camera *J. Appl. Clin. Med. Phys.* **18** 210–9
- Archambault L, Poenisch F, Sahoo N, Robertson D, Lee A, Gillin M T, Mohan R and Beddar S 2012 Verification of proton range, position, and intensity in IMPT with a 3D liquid scintillator detector system *Med. Phys.* **39** 1239–46
- Archambault L, Polf J C, Beaulieu L and Beddar S 2008 Characterizing the response of miniature scintillation detectors when irradiated with proton beams *Phys. Med. Biol.* **53** 1865
- Arjomandy B, Sahoo N, Ciangaru G, Zhu R, Song X and Gillin M 2010 Verification of patient-specific dose distributions in proton therapy using a commercial two-dimensional ion chamber array *Med. Phys.* **37** 5831–7
- Baldock C, Deene Y D, Doran S, Ibbott G, Jirasek A, Lepage M, McAuley K B, Oldham M and Schreiner L J 2010 Polymer gel dosimetry *Phys. Med. Biol.* **55** R1
- Beaulieu L and Beddar S 2016 Review of plastic and liquid scintillation dosimetry for photon, electron, and proton therapy *Phys. Med. Biol.* **61** R305
- Beddar A S, Mackie T R and Attix F H 1992a Cerenkov light generated in optical fibres and other light pipes irradiated by electron beams *Phys. Med. Biol.* **37** 925
- Beddar A S, Mackie T R and Attix F H 1992b Water-equivalent plastic scintillation detectors for high-energy beam dosimetry: I. Physical characteristics and theoretical considerations *Phys. Med. Biol.* **37** 1883
- Beddar A S, Mackie T R and Attix F H 1992c Water-equivalent plastic scintillation detectors for high-energy beam dosimetry: II. Properties and measurements *Phys. Med. Biol.* **37** 1901
- Beddar S, Archambault L, Sahoo N, Poenisch F, Chen G T, Gillin M T and Mohan R 2009 Exploration of the potential of liquid scintillators for real-time 3D dosimetry of intensity modulated proton beams *Med. Phys.* **36** 1736–43
- Birks J B 1964 *The Theory and Practice of Scintillation Counting: International Series of Monographs in Electronics and Instrumentation* (Pergamon)
- Blanc D, Cambou F and De Lafond Y G 1964 Kinetics of the fast component of scintillation in a pure organic medium *comptes rendus de l'académie des sciences* 3187
- Boivin J, Beddar S, Bonde C, Schmidt D, Culberson W, Guillemette M and Luc Beaulieu 2016 A systematic characterization of the low-energy photon response of plastic scintillation detectors *Phys. Med. Biol.* **61** 5569
- Bouguet J 2010 *Camera Calibration Toolbox for MATLAB* (Pasadena, CA: California Institute of Technology)

- Chou C N 1952 The Nature of the Saturation Effect of Fluorescent Scintillators *Phys. Rev.* **87** 904–5
- Christensen J B and Andersen C E 2018 Relating ionization quenching in organic plastic scintillators to basic material properties by modelling excitation density transport and amorphous track structure during proton irradiation *Phys. Med. Biol.* Online: <http://iopscience.iop.org/10.1088/1361-6560/aadf2d>
- Collomb-Patton V, Boher P, Leroux T, Fontbonne J-M, Vela A and Batalla A 2009 The DOSIMAP, a high spatial resolution tissue equivalent 2D dosimeter for LINAC QA and IMRT verification *Med. Phys.* **36** 317–28
- Coray A, Pedroni E, Boehringer T, Lin S, Lomax T and Goitein G 2002 Dosimetry with the scanned proton beam on the PSI gantry Online: http://inis.iaea.org/Search/search.aspx?orig_q=RN:34017937
- Darne C D, Alsanea F, Robertson D G, Sahoo N and Beddar S 2017 Performance characterization of a 3D liquid scintillation detector for discrete spot scanning proton beam systems *Phys. Med. Biol.* **62** 5652
- Darne C, Robertson D, Alsanea F and Beddar S 2016 SU-D-BRC-07: System Design for a 3D Volumetric Scintillation Detector Using SCMOS Cameras *Med. Phys.* **43** 3337–3337
- Doran S, Gorjiara T, Kacperek A, Adamovics J, Kuncic Z and Baldock C 2015 Issues involved in the quantitative 3D imaging of proton doses using optical CT and chemical dosimeters *Phys. Med. Biol.* **60** 709
- Durante M and Paganetti H 2016 Nuclear physics in particle therapy: a review *Rep. Prog. Phys.* **79** 096702
- Fukushima Y, Hamada M, Nishio T and Maruyama K 2006 Development of an easy-to-handle range measurement tool using a plastic scintillator for proton beam therapy *Phys. Med. Biol.* **51** 5927
- Gillin M T, Sahoo N, Bues M, Ciangaru G, Sawakuchi G, Poenisch F, Arjomandy B, Martin C, Titt U, Suzuki K, Smith A R and Zhu X R 2010 Commissioning of the discrete spot scanning proton beam delivery system at the University of Texas M.D. Anderson Cancer Center, Proton Therapy Center, Houston *Med. Phys.* **37** 154–63
- Hitachi A, Doke T and Mozumder A 1992 Luminescence quenching in liquid argon under charged-particle impact: Relative scintillation yield at different linear energy transfers *Phys. Rev. B* **46** 11463–70
- Hui C K, Robertson D, Alsanea F and Beddar S 2015 Fast range measurement of spot scanning proton beams using a volumetric liquid scintillator detector *Biomed. Phys. Eng. Express* **1** 025204
- Hui C, Robertson D and Beddar S 2014 3D reconstruction of scintillation light emission from proton pencil beams using limited viewing angles—a simulation study *Phys. Med. Biol.* **59** 4477
- Ingram W S, Robertson D and Beddar S 2015 Calculations and measurements of the scintillator-to-water stopping power ratio of liquid scintillators for use in proton radiotherapy *Nucl. Instrum. Methods Phys. Res. Sect. Accel. Spectrometers Detect. Assoc. Equip.* **776** 15–20

- Jordan K 2010 Review of recent advances in radiochromic materials for 3D dosimetry *J. Phys. Conf. Ser.* **250** 012043
- Kanaya K and Okayama S 1972 Penetration and energy-loss theory of electrons in solid targets *J. Phys. Appl. Phys.* **5** 43
- Karger C P, Jäkel O, Hartmann G H and Heeg P 1999 A system for three-dimensional dosimetric verification of treatment plans in intensity-modulated radiotherapy with heavy ions *Med. Phys.* **26** 2125–32
- Karger C P, Jäkel O, Palmans H and Kanai T 2010 Dosimetry for ion beam radiotherapy *Phys. Med. Biol.* **55** R193
- Kooy H M and Grassberger C 2015 Intensity modulated proton therapy *Br. J. Radiol.* **88** 20150195
- Kroll F, Pawelke J and Karsch L 2013 Preliminary investigations on the determination of three-dimensional dose distributions using scintillator blocks and optical tomography *Med. Phys.* **40** 082104
- Lepage M and Jordan K 2010 3D dosimetry fundamentals: gels and plastics *J. Phys. Conf. Ser.* **250** 012055
- Létourneau D, Gulam M, Yan D, Oldham M and Wong J W 2004 Evaluation of a 2D diode array for IMRT quality assurance *Radiother. Oncol.* **70** 199–206
- Lomax A J, Böhringer T, Bolsi A, Coray D, Emert F, Goitein G, Jermann M, Lin S, Pedroni E, Rutz H, Stadelmann O, Timmermann B, Verwey J and Weber D C 2004 Treatment planning and verification of proton therapy using spot scanning: Initial experiences *Med. Phys.* **31** 3150–7
- Michaelian K and Menchaca-Rocha A 1994 Model of ion-induced luminescence based on energy deposition by secondary electrons *Phys. Rev. B* **49** 15550–62
- Michaelian K, Menchaca-Rocha A and Belmont-Moreno E 1995 Scintillation response of nuclear particle detectors *Nucl. Instrum. Methods Phys. Res. Sect. Accel. Spectrometers Detect. Assoc. Equip.* **356** 297–303
- Michaelian K, Menchaca-Rocha A and Hilarion S 1997 Ion-induced luminescence *J. Lumin.* **72–74** 740–1
- Moomaw B 2013 Chapter 11 - Camera Technologies for Low Light Imaging: Overview and Relative Advantages *Methods in Cell Biology Digital Microscopy* vol 114, ed G Sluder and D E Wolf (Academic Press) pp 243–83 Online: <http://www.sciencedirect.com/science/article/pii/B9780124077614000117>
- Nikjoo H, Uehara S, Emfietzoglou D and Cucinotta F A 2006 Track-structure codes in radiation research *Radiat. Meas.* **41** 1052–74
- Paganetti H 2011 *Proton Therapy Physics* vol 20115763 (CRC Press) Online: <http://www.crcnetbase.com/doi/book/10.1201/b11448>
- Pawlicki T, Dunscombe P, Mundt A J and Scalliet P 2010 *Quality and safety in radiotherapy* (CRC Press)

- Pedroni E, Scheib S, Böhringer T, Coray A, Grossmann M, Lin S and Lomax A 2000 *Absorbed Dose Determination in External Beam Radiotherapy* (Vienna: IAEA)
- Petric M P, Robar J L and Clark B G 2006 Development and characterization of a tissue equivalent plastic scintillator based dosimetry system *Med. Phys.* **33** 96–105
- Platt J R 1949 Classification of Spectra of Cata-Condensed Hydrocarbons *J. Chem. Phys.* **17** 484–95
- Pönisch F, Archambault L, Briere T M, Sahoo N, Mohan R, Beddar S and Gillin M T 2009 Liquid scintillator for 2D dosimetry for high-energy photon beams *Med. Phys.* **36** 1478–85
- Poppe B, Blechschmidt A, Djouguela A, Kollhoff R, Rubach A, Willborn K C and Harder D 2006 Two-dimensional ionization chamber arrays for IMRT plan verification *Med. Phys.* **33** 1005–15
- Robertson D G 2014 Volumetric scintillation dosimetry for scanned proton beams
- Robertson D, Hui C, Archambault L, Mohan R and Beddar S 2014 Optical artefact characterization and correction in volumetric scintillation dosimetry *Phys. Med. Biol.* **59** 23–42
- Robertson D, Mirkovic D, Sahoo N and Beddar S 2013 Quenching correction for volumetric scintillation dosimetry of proton beams *Phys. Med. Biol.* **58** 261
- Russo S, Mirandola A, Molinelli S, Mastella E, Vai A, Magro G, Mairani A, Boi D, Donetti M and Ciocca M 2017 Characterization of a commercial scintillation detector for 2-D dosimetry in scanned proton and carbon ion beams *Phys. Med.* **34** 48–54
- Sawakuchi G O, Mirkovic D, Perles L A, Sahoo N, Zhu X R, Ciangaru G, Suzuki K, Gillin M T, Mohan R and Titt U 2010 An MCNPX Monte Carlo model of a discrete spot scanning proton beam therapy nozzle *Med. Phys.* **37** 4960–70
- Schreiner L J 2015 True 3D chemical dosimetry (gels, plastics): Development and clinical role *J. Phys. Conf. Ser.* **573** 012003
- Smith A, Gillin M, Bues M, Zhu X R, Suzuki K, Mohan R, Woo S, Lee A, Komaki R, Cox J, Hiramoto K, Akiyama H, Ishida T, Sasaki T and Matsuda K 2009 The M. D. Anderson proton therapy system *Med. Phys.* **36** 4068–83
- Tobias C A, Lawrence J H, Born J L, McCombs R K, Roberts J E, Anger H O, Low-Beer B V A and Huggins C B 1958 Pituitary Irradiation with High-Energy Proton Beams A Preliminary Report *Cancer Res.* **18** 121–34
- Torrisi L 2000 Plastic scintillator investigations for relative dosimetry in proton-therapy *Nucl. Instrum. Methods Phys. Res. Sect. B Beam Interact. Mater. At.* **170** 523–30
- Wang L L W, Perles L A, Archambault L, Sahoo N, Mirkovic D and Beddar S 2012 Determination of the quenching correction factors for plastic scintillation detectors in therapeutic high-energy proton beams *Phys. Med. Biol.* **57** 7767–81
- Wilson R R 1946 Radiological Use of Fast Protons *Radiology* **47** 487–91

Xu X G, Bednarz B and Paganetti H 2008 A review of dosimetry studies on external-beam radiation treatment with respect to second cancer induction *Phys. Med. Biol.* **53** R193

Zhu X R, Poenisch F, Song X, Johnson J L, Ciangaru G, Taylor M B, Lii M, Martin C, Arjomandy B, Lee A K, Choi S, Nguyen Q nhu, Gillin M T and Sahoo N 2011 Patient-Specific Quality Assurance for Prostate Cancer Patients Receiving Spot Scanning Proton Therapy Using Single-Field Uniform Dose *Int. J. Radiat. Oncol.* **81** 552–9

Zhu X R, Sahoo N, Zhang X, Robertson D, Li H, Choi S, Lee A K and Gillin M T 2010 Intensity modulated proton therapy treatment planning using single-field optimization: The impact of monitor unit constraints on plan quality *Med. Phys.* **37** 1210–9

Vita

Fahed M Alsanea was born in Kuwait City, Kuwait. After graduating from Alrujaib High School, Bayan, Kuwait in 2007, he moved to the United States and entered Virginia Commonwealth University in Richmond, Virginia. He received the degree of Bachelor of Science from VCU in May, 2012. For the next two years, he worked at Purdue University as graduate research assistant and earned a master's degree in medical physics. In August of 2014 he entered The University of Texas MD Anderson Cancer Center UTHealth Graduate School of Biomedical Sciences.

Permanent address:

825 Orlando Dr
Fort Wayne, Indiana 46825